

## Autonomous Surface Vehicle Measurements of the Ocean's Response to Tropical Cyclone Freda

LUC LENAIN AND W. KENDALL MELVILLE

*Scripps Institution of Oceanography, University of California, San Diego, La Jolla, California*

(Manuscript received 15 January 2014, in final form 14 April 2014)

### ABSTRACT

On 31 December 2012, an instrumented autonomous surface vehicle (ASV; Wave Glider) transiting across the Pacific from Hawaii to Australia as part of the Pacific Crossing (PacX) project came very close (46 km) to the center of a category 3 Tropical Cyclone (TC), Freda, experiencing winds of up to  $37 \text{ m s}^{-1}$  and significant wave heights close to 10 m. The Wave Glider was instrumented for surface ocean–lower atmosphere (SOLA) measurements, including atmospheric pressure, surface winds and temperature, sea surface temperature, salinity, dissolved oxygen, fluorescence (chlorophyll-*a* and turbidity), and surface-wave directional spectra. Such measurements in close proximity to a tropical cyclone are rare. This study presents novel observations of the ocean's response in three quadrants of TC Freda, collected from the instrumented glider. Evolution of the wind, the directional wave field, the sea surface temperature, and the Stokes drift profile (calculated from the wave directional spectrum) as Freda passed near the vehicle are examined. Results are discussed in the context of the recent coupled wind-wave modeling and large eddy simulation (LES) modeling of the marine boundary layer in Hurricane Frances (Sullivan et al. 2012). Processes by which cold nutrient-rich waters are entrained and mixed from below into the mixed layer as the TC passes near the Wave Glider are presented and discussed. The results of this encounter of an autonomous surface vehicle with TC Freda supports the use of ASVs for regular TC (hurricane) monitoring to complement remote sensing and “hurricane hunter” aircraft missions.

### 1. Introduction

Hurricanes, otherwise known as tropical cyclones (TC) or typhoons, are among the most destructive natural phenomena impacting the oceans and coastal waters. Tropical cyclone intensity, characterized by the Saffir–Simpson scale of sustained winds, is a key parameter that ultimately helps define the potential impact of the surface winds, the extent of storm surge, and the depth of upper-ocean mixing. While forecasting the track of tropical cyclones has significantly improved in recent decades, TC intensity forecasts remain uncertain in a context where climate models suggest an increase in the frequency of intense TCs (Bender et al. 2007).

A number of studies have aimed to improve our understanding of tropical cyclone genesis and dynamics (Price 1981; D'Asaro et al. 2006; Black et al. 2007; D'Asaro et al. 2007; Sanford et al. 2007, 2011a,b; Bell et al. 2012; Mrvaljevic et al. 2013). One of the challenges in this area of air–sea interaction research is the lack of in situ measurements in close proximity to these intense storms. Past studies have often been limited to using remote sensing products and air-launched instrumentation (Powell et al. 2003; Sanford et al. 2011b). Very few of those measurement campaigns collected a combination of atmospheric, surface dynamics, and oceanographic measurements at the same time and location.

Though a significant number of one-dimensional wave spectra and samples of wave statistics in TCs have been collected over the past couple of decades (Young 2003, 2006), wave directional spectra remain sparse (Young 2006) and are often constrained to radar-based airborne wave mapping techniques that better resolve the longer waves (Walsh et al. 1985; Moon et al. 2003; Black et al. 2007). In addition, the sampling of the lower part of the marine atmospheric boundary layer (MABL) in those intense storms

---

 Denotes Open Access content.

---

Corresponding author address: L. Lenain, Scripps Institution of Oceanography, 9500 Gilman Dr., La Jolla, CA 92093-0213.  
E-mail: llenain@ucsd.edu

DOI: 10.1175/JTECH-D-14-00012.1

© 2014 American Meteorological Society

is often only achievable using limited air-launched instrumentation like GPS dropsondes (Powell et al. 2003). Measuring the evolution of the wave directional spectrum in a tropical storm is critical for improving hurricane intensity forecasts, as the Stokes drift of the surface wave field interacting with the vorticity of surface shear currents produces Langmuir circulations (LCs) through the vortex force of the Craik–Leibovich theory (Craik and Leibovich 1976). LCs contribute to the mixing of the upper ocean and hence to the enthalpy transfer between the ocean and the atmosphere (Sullivan and McWilliams 2010; Sullivan et al. 2012) through contributions to entrainment of cooler water from below by “Langmuir turbulence” and shear associated with strong currents in the wake of the storm (D’Asaro et al. 2007; Sanford et al. 2007).

In this paper, we present oceanographic and atmospheric boundary layer data collected from an instrumented unmanned surface vehicle [USV; Wave Glider (WG), Liquid Robotics] as it passed near the category 3 Tropical Cyclone Freda.

The Pacific Crossing (PacX) project, to send Wave Gliders across the Pacific from California to Australia and Asia, was not designed as a tropical cyclone science program, but the serendipitous availability of the rare data that were gathered, while limited, supports recent hurricane modeling results and opens a window to the development of improved methods of measuring surface ocean–lower atmosphere (SOLA) processes in tropical cyclones. Evolution of the wind, the directional wave field, and estimates of the Stokes drift profile are presented and discussed. The outline of the paper is as follows. In section 2 the Wave Glider and its instrumentation are described. In section 3 we briefly describe TC Freda. In section 4 we present the measurements of the SOLA response to Freda. In section 5 we present evidence of the ocean’s biophysical response to the TC, and in section 6 we summarize and discuss our findings.

## 2. The instrumented Wave Glider

The Liquid Robotics (LR, Sunnyvale, California) Wave Glider is a novel ocean-wave-propelled autonomous surface vehicle (ASV) with a two-body design. The lower part, called the “glider” is tethered to the surface “float” section of the vehicle by an approximately 7-m-long umbilical cable. The fins installed on the glider convert the orbital motion of the wave into a horizontal force (much the same way as personal swim fins do) that tows the instrumented surface float. Though the Wave Glider’s propulsion system is purely mechanical, there are two solar panels mounted on the float to supply power for the navigation and communication systems and onboard instrumentation.

Wave Gliders are controlled and navigated using an Iridium satellite link back to shore. Waypoints are sent to the vehicle using the Wave Glider Management System (WGMS), proprietary Liquid Robotics control software. Details about the vehicle design and performance are provided in Table 1.

### a. PacX experiment

In November of 2011, Liquid Robotics launched the PacX experiment, sending four Wave Gliders across the Pacific Ocean to demonstrate the endurance and reliability of their vehicles. The four Wave Gliders left from San Francisco, California, and first transited to Hawaii. From there, two vehicles headed to Australia and two to Japan. One of the two Wave Gliders heading to Australia, *WG Benjamin*, named in honor of the early American scientist and Gulf Stream pioneer, Benjamin Franklin, came in close proximity to the category 3 Tropical Cyclone Freda.

### b. Instrumentation

Liquid Robotics fitted all four Wave Gliders with a suite of atmospheric and oceanographic instruments. Figure 1 shows a picture of the instrumented glider during engineering tests off the western coast of the island of Hawaii prior to the start of the PacX project. An Airmar (Milford, New Hampshire) PB200 sensor was installed to measure air temperature, barometric pressure, wind speed, wind gust speed, and wind direction 1 m above the deck of the Wave Glider. Data were sampled at 1 Hz and then averaged over a 10-min window before being transmitted back to shore through Iridium communications.

The wave field was characterized using a Datawell (Haarlem, The Netherlands) MOSE G-1000 wave sensor installed on the glider float. This sensor produces three-component displacements in a fixed north–east–vertical coordinate frame using a high-accuracy GPS receiver-based system that measures the horizontal and vertical buoy velocities based on the Doppler shift in received GPS signals. These velocities are then integrated internally in the unit to produce north–east–vertical displacement time series. The standard Datawell output products (bulk wave parameters, frequency spectra) were streamed back to shore, while the continuous 2-Hz time series were logged internally and recovered once *WG Benjamin* reached its final destination in Australia. All spectra considered in the analysis reported here were reprocessed using the raw 2-Hz data stream to account for the brief loss of GPS signal during heavy seas that may have been caused by occasional submergence of the antenna under breaking waves. As described in appendix A, since the Wave Glider is not optimally designed as a wave buoy, the wave-measuring

TABLE 1. Liquid Robotics WG specifications. Circular error probability (CEP), World Meteorological Organization (WMO); 1 kt = 0.51 ms<sup>-1</sup>.

Dimensions	Float (length × width): 208 cm × 60 cm Underwater glider, at 7-m depth (height × length): 40 cm × 191 cm Wings: 107 cm wide
Weight (dry)	Mass: 90 kg
Buoyancy (in water)	Displacement: 150 kg
Endurance	Up to 1 year (variable)
Speed in water	0.4–2 kt (variable)
Depth rating	Continuous wash and salt spray Brief submergence to 2 m
Propulsion	Mechanical conversion of wave energy into forward propulsion
Battery	665 watt-hours–lithium-ion rechargeable
Solar power	80 W (peak) for battery charging, onboard electronics, and payloads
Command and control power	1.5 W continuous
Available payload power	10 A (max) continuous at 13.2 V
Communication	Iridium and 2.4 GHz
Navigation accuracy	3-m radius CEP50
Station keeping	40-m radius CEP90 in WMO sea state 3 (with current < 0.5 kt)

Wave Glider system was tested against a separate Datawell directional wave buoy.

A Sea-Bird Electronics (Bellevue, Washington) water conductivity–temperature–depth (CTD) and dissolved oxygen sensor was installed at the base of the float. The Glider Payload CTD (GPCTD) is specifically designed for use on autonomous platforms. It is a self-contained CTD equipped with onboard memory and storage, and integrated pump with low power consumption and small form factor. A flow-controlled dissolved oxygen (DO) sensor was added directly in line with the T and C sensors. A collocated pressure sensor provides depth information. The GPCTD is designed to minimize power consumption. During the PacX experiment, the instrument was set to burst sample at 10-s intervals over 70 s every 10 min. A Turner Designs (Sunnyvale) C3 fluorometer designed to measure chlorophyll-*a* in vivo fluorescence [460-nm excitation and 696-nm emission wavenumber, raw fluorescence units (RFU)], turbidity [850-nm excitation and 850-nm emission, nephelometric turbidity units (NTU)], and crude oil material (325-nm excitation and 410–600-nm emission) was also installed below the glider float. The sampling interval was set to 2 min. The sensor was calibrated before and after the PacX experiment following the manufacturer's recommendations.

#### c. Remote sensing products

In addition to the in situ measurements, remote sensing products were also available in the present study. We used the Multiplatform Tropical Cyclone Surface Wind Analysis (MTCSWA) dataset, an operational product

available through the National Oceanic and Atmospheric Administration (NOAA) National Environmental Satellite, Data, and Information Service (NESDIS) and the Regional and Mesoscale Meteorology Branch (RAMMB) at Colorado State University, Fort Collins, Colorado. Global tropical cyclone surface and flight-level wind analyses are produced every 6 h, through objective mapping of remotely sensed winds from satellites (Knaff et al. 2011).

#### d. Numerical model

Numerical products (significant wave height, surface winds) publicly available from the combined Joint Typhoon Warning Center WAVEWATCH III (JTWC/W3) model were also used in the present study. The model uses a modified Navy Operational Global Atmospheric Prediction System (NOGAPS) wind field forecast, using a JTWC estimate of the storm (radius of maximum winds, and radius of the outermost closed isobar to characterize the extent of the TC circulation), which is then used as input to WAVEWATCH III to improve wave height forecasts (Sampson et al. 2010, 2013).

### 3. TC Freda

Freda became a tropical depression on 26 December 2012, forming approximately 295 km northeast of the Solomon Islands in the western Pacific. The system quickly became a tropical cyclone on 29 December 2012, tracking along the northwestern edge of a subtropical atmospheric ridge in a southwesterly direction. It continued intensifying

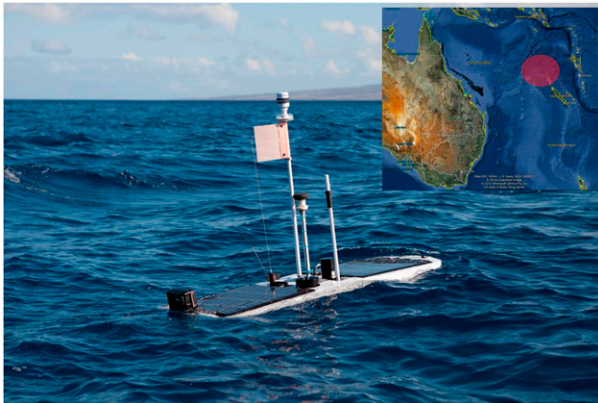


FIG. 1. Wave Glider *Benjamin* during engineering tests off the island of Hawaii, prior to the PacX deployment. The insert shows the geographical area where the glider encountered Tropical Cyclone Freda, on 31 Dec 2012, northwest of New Caledonia.

and reached category 3 intensity on 30 December shortly after crossing  $161^{\circ}\text{E}$ , with winds reaching up to  $55\text{ m s}^{-1}$ , and a measured pressure of 975 mbar. The cyclone later weakened because of strong wind shear, was downgraded to a tropical storm on 1 January 2013, and then was just a low pressure area on 2 January 2013 before it struck New Caledonia.

#### 4. Ocean response to TC Freda

Figure 2 shows Freda's track and intensity ( $\text{m s}^{-1}$ ) from 1200 UTC 28 December 2012 through 1200 UTC 4 January 2013. Also shown is the WG *Benjamin* track, getting as close as 46 km from the center of the eye at 1200 UTC 31 December 2012. The storm quickly weakened once it passed south of the Wave Glider. Also note that WG *Benjamin* was set to be on a constant westerly heading during the storm. The shape of the glider track once it reached the wake of the TC implies very strong westerly then northward surface currents that swept the glider into the wake of the storm.

The relative distance between the WG and the center of the storm is shown in Fig. 3a. It was able to continuously collect data in three quadrants of the TC. Figures 3b and 3c show the eastward and northward, respectively, glider (blue) and surface current (red) velocity components. Unfortunately, the surface velocity sensor used for navigation purposes was turned off from 1030 UTC 31 December 2012 to 1915 UTC 1 January 2013 to reduce payload power consumption. During the same period of time, once the WG reached the wake of the TC in quadrant C, platform speed over ground (GPS SOG) of up to  $1.5\text{ m s}^{-1}$  was measured, moving toward the east, in the direction opposite to its navigational setting, implying the existence of opposing near-surface currents of even greater amplitude.

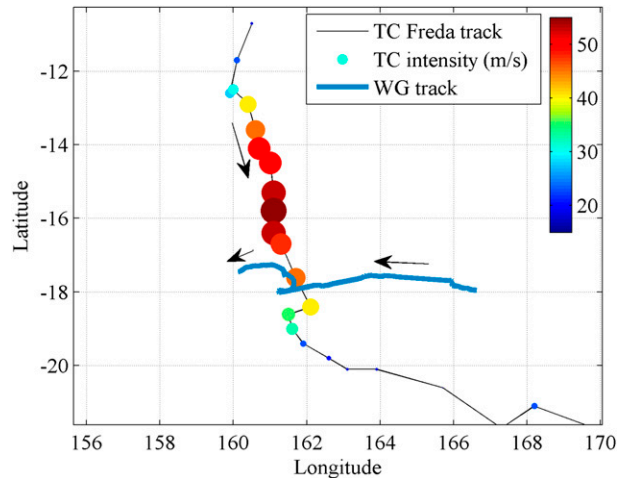


FIG. 2. Track and intensity (peak winds, color coded;  $\text{m s}^{-1}$ ) of TC Freda (black line) and track of WG *Benjamin* (blue), from 28 Dec 2012 through 4 Jan 2013. Note that the diameter of the circles is proportional to the storm's intensity.

Figure 4 shows the evolution of the main parameters of the MABL and surface conditions from 25 December 2012 through 1 January 2013 as the WG passed near the eye of the TC. Each data point represents a 10-min average. Figure 4a shows the barometric pressure. As expected, the lowest value was recorded near the center of the TC, reaching almost 975 mbar. Figure 4b shows the significant wave height  $H_s$  measured from the Datawell sensor and the estimate from the JTWC/W3 numerical forecast at the WG location. Here  $H_s$  is defined as  $H_s = 4 \cdot \langle \eta^2 \rangle$ , where  $\eta(t)$  is the surface displacement and  $\langle \cdot \rangle$  denotes the 10-min average. The significant wave height rapidly increased as the WG got closer to the eye of the TC, reaching 9.9 m at 1400 UTC 31 December 2013. Figure 4c shows the wind speed measured by the glider at 1 m above the water surface, the spatially interpolated wind products from JTWC/W3 and MTCSSWA, and the wind speed at 10-m height  $U_{10}$  extrapolated from the WG sonic anemometer at 1 m, computed iteratively using Tropical Ocean and Global Atmosphere Coupled Ocean–Atmosphere Response Experiment 3.0 (TOGA COARE 3.0) algorithm (Fairall et al. 2003) assuming a constant flux layer with a logarithmic wind profile:

$$U_{10} = \frac{u_{*a}}{\kappa} \ln\left(\frac{10}{z_o}\right), \quad (1)$$

where  $u_{*a}$  is the friction velocity in the air and  $z_o$  is the roughness length as described in Fairall et al. (2003):

$$z_o = \frac{\alpha u_{*a}^2}{g} + \frac{0.11\nu}{u_*}, \quad (2)$$

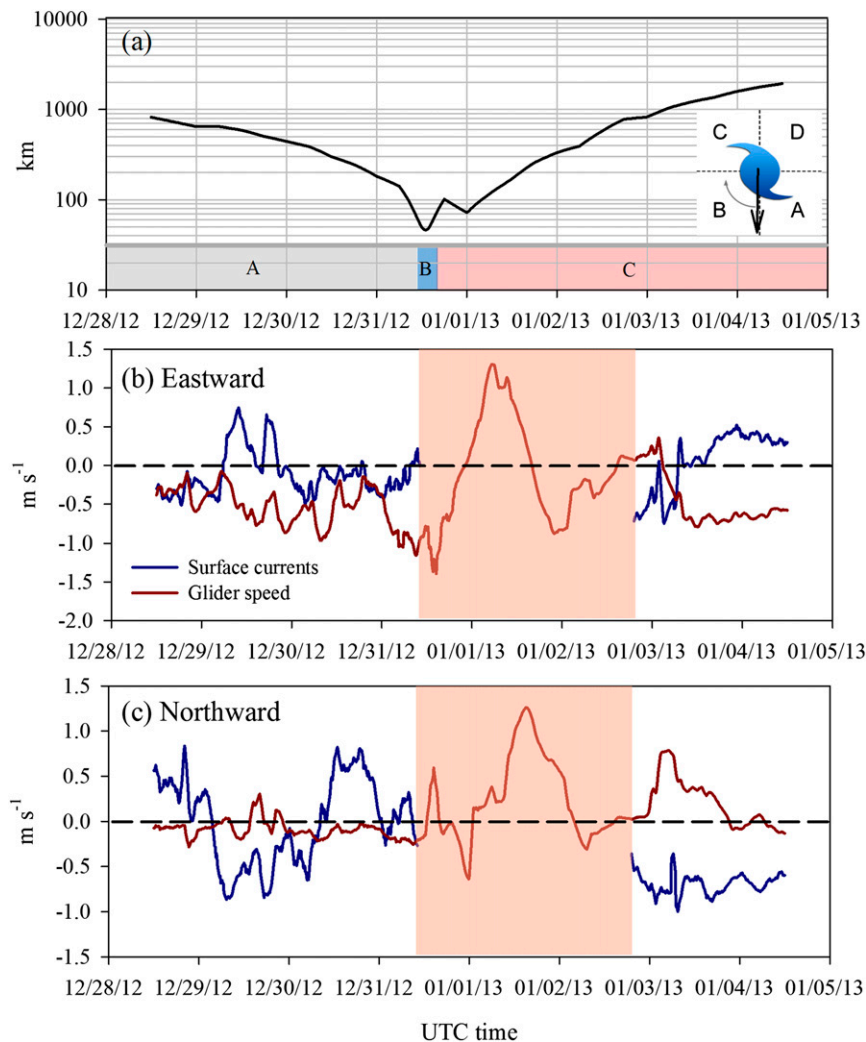


FIG. 3. (a) Distance between the glider and eye of TC Freda, as estimated by the JTWC, as a function of time. Also highlighted are the quadrant locations of the WG, relative to TC Freda as defined in the insert. (b), (c) Eastward- and northward-measured surface currents (blue) and WG GPS speed over ground (red). The surface velocity sensor was unfortunately turned off at 1030 UTC 31 Dec 2012 until 1915 UTC 1 Jan 2013 to reduce power consumption; the shaded areas in (b) and (c).

where  $\nu$  is the kinematic viscosity and  $\alpha$  is Charnock's parameter (Charnock et al. 1955).

Figure 4d shows the corresponding wind (from) direction relative to true north. Average wind speed quickly increased to  $36.5 \text{ m s}^{-1}$  near the center of the TC, at 1400 UTC 31 December 2012. The wind direction shifted from  $100^\circ$  to  $280^\circ$  over the course of 24 h starting on 31 December 2012 as the WG passed through three quadrants of the TC. The wind direction from the JTWC/W3 and MTCSWA products are in relatively good agreement with the measured wind direction, while the wind speed from the JTWC/W3 product is in good agreement up to the peak of the storm and then diverges significantly. The MTCSWA surface wind product is in

poor agreement with the in situ measurement up to 1 January 2013, when it starts to improve significantly. The discrepancy is likely caused by inaccuracies in the TC intensity forecast because of limitations of the JTWC and MTCSWA algorithm (Knaff et al. 2013; J. Knaff 2013, personal communication). We also found that the JTWC/W3 wave product did a poor job reproducing the significant wave height along the track of the Wave Glider. Figure 4e shows sea surface temperature (SST) and conductivity measured from the GPCTD mounted at the base of the float. Both SST and conductivity decreased significantly once the glider reached the wake of the TC, as reported in previous studies (D'Asaro et al. 2007; Mrvaljevic et al. 2013).

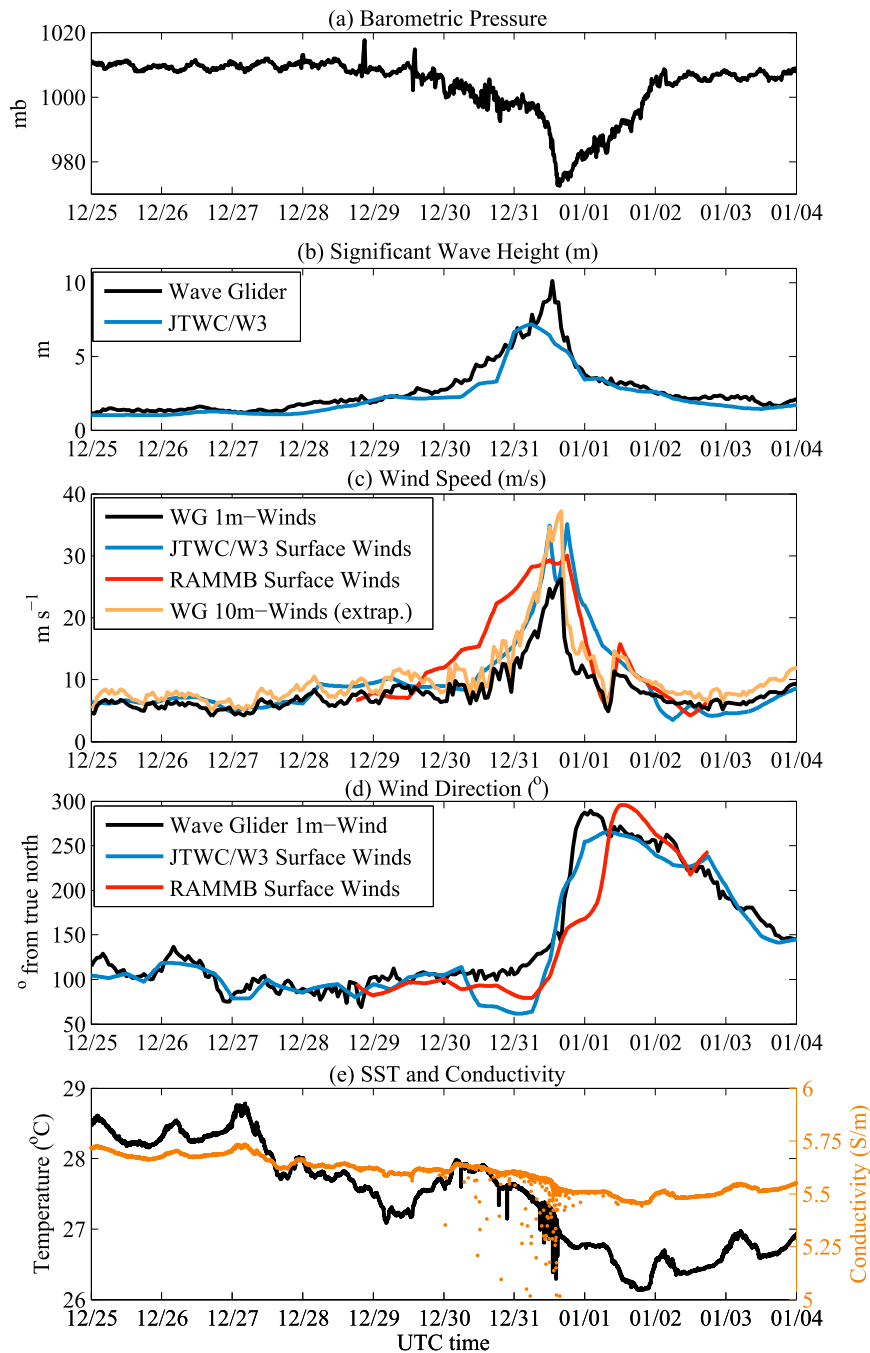


FIG. 4. Environmental conditions measured by the WG during TC Freda. (a) Barometric pressure, (b) significant wave height, (c) wind speed ( $\text{m s}^{-1}$ ; black: WG  $U_1$  measured at 1-m height, blue: surface winds from JTWC/W3 product, red: RAMMB, reanalyzed surface winds, and orange: WG  $U_{10}$  estimated from  $U_1$ ), (d) wind direction (coming from relative to true north), and (e) sea surface temperature ( $^{\circ}\text{C}$ ) and conductivity ( $\text{S m}^{-1}$ ). Noise in conductivity measurements in high wind and wave conditions may be due to near-surface bubble clouds (cf. Lamarre and Melville 1991).

Figure 5 shows an example time series of sea surface displacement collected around 1540 UTC 31 December 2012. The horizontal velocity in the mean wave direction for that period of time (coming from  $150^{\circ}$ , relative to

true north) is shown as color-coded dots. At that time, the significant wave height  $H_s = 7.5 \text{ m}$  and the wind speed  $U_{10} = 36.5 \text{ m s}^{-1}$ . A couple of extreme waves, sometimes called “rogue” waves, were measured by the

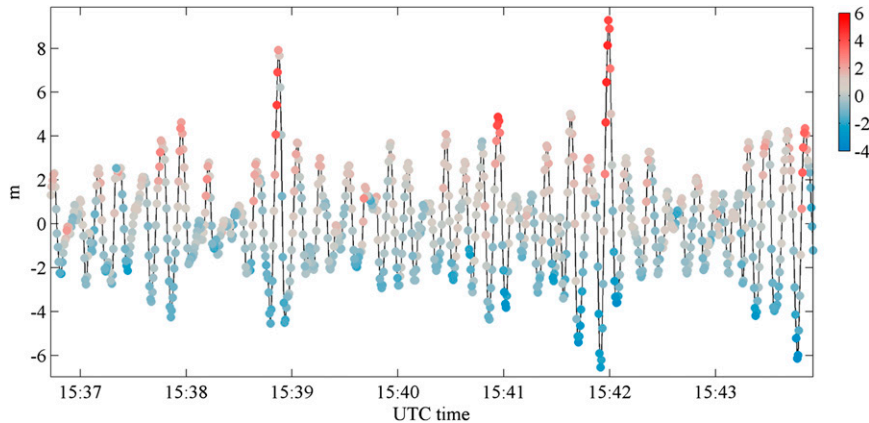


FIG. 5. Example time series of sea surface displacement measured by the WG around 1540 UTC 31 Dec 2013. The measured glider horizontal velocity in the mean wave direction is shown as color-coded dots ( $\text{m s}^{-1}$ ). Significant wave height  $H_s$  was equal to 7.5 m and wind speed  $U_{10}$  was equal to  $36.5 \text{ m s}^{-1}$  at the time of measurement. Note that the largest wave, at 1542 UTC, has a height exceeding  $2H_s$ .

WG, the largest one appeared at 1542 UTC. Peak-to-peak height was 15.83 m, with a maximum WG horizontal velocity of  $4.8 \text{ m s}^{-1}$ .

The spectrogram of the sea surface displacement is shown in Fig. 6. The spectra were computed using 256-s FFT windows with 50% overlap over a 30-min record. Low-frequency swell (20–25-s period) appeared on 26 December 2012 while the TC was still a significant distance from the WG and its period slowly decreased as the TC got closer. On 30 December 2012, wind waves became dominant as the wind quickly increased, ultimately reaching speeds close to  $27 \text{ m s}^{-1}$  (at 1 m above the surface, equivalent to  $36.5 \text{ m s}^{-1}$  at 10 m) at the peak of the storm. The evolution of the wave frequency spectrum is shown in Fig. 7. Spectra are color coded for wind speed at 1-m height. The evolution of the spectral shape as the wind increases is consistent with the measurements by Donelan et al. (1985) and Young (2006). While a low-frequency swell peak is present at the lowest wind speed, where the measurements were collected at a significant distance from the TC, the wave spectrum quickly becomes unimodal as the wind increased and the glider got closer to the center of the TC.

For each 30-min record, the directional wave spectrum  $S_{f\theta}$  is computed using the Wave Analysis for Fatigue and Oceanography (WAFO) MATLAB library (Brodtkorb et al. 2000) using the horizontal (north, east) and vertical displacements of the glider float. Figure 8 presents the evolution of the directional wave field as the TC passed near the WG. The relative storm location is qualitatively depicted by a hurricane symbol. The red arrow represents the wind vector, while the directional wave information uses the “from” direction. The first sign of the approaching storm occurs on 30 December 2012, in the form of

a northerly swell, while the high-frequency part of the spectrum is dominated by westerly wind waves. As the TC got closer to the WG, at 0900 31 December 2012, the energy associated with the swell and wind waves increased, with 1-m winds reaching close to  $19.5 \text{ m s}^{-1}$ , still showing a sharp bimodal distribution of wave energy. A few hours later, as the TC gets even closer to the WG and the wind increased (1-m wind  $U_1 = 24.7 \text{ m s}^{-1}$ ), the swell and wind wave energy start converging into a single, broader energy peak, effectively transitioning from a bimodal to a unimodal spectrum. The directional spread of energy at the peak frequency is significant, driven by the rapid change in wind direction as the glider passed through the right (west) side of the TC, relative to the direction of TC propagation. A few hours later, at 1600 UTC, when the WG was located directly to the right (west) of the eye of the TC, the spectrum was dominated by wind-generated waves, coming from the southeast. Wind speed rapidly decreased once the glider reached the TC wake, with the 1-m wind speed,  $U_1$ , only  $11.6 \text{ m s}^{-1}$  at 2000 UTC 31 December 2012, coming from the southwest. Note that the wind and peak wave directions are not perfectly aligned, as the wave field does not have time to reach wind-wave equilibrium in such a rapidly varying environment.

Spatial variability of the wind speed and significant wave height is depicted in Fig. 9, where the measurement location used is the relative distance (km) in an earth coordinate frame between the WG and the eye of the TC. The mean direction of propagation of Freda is shown as a black arrow. Note the rapid increase in wind and wave conditions as the storm passed to the east of the WG and the sharp change in wind direction as the WG encounters the wake of the TC.

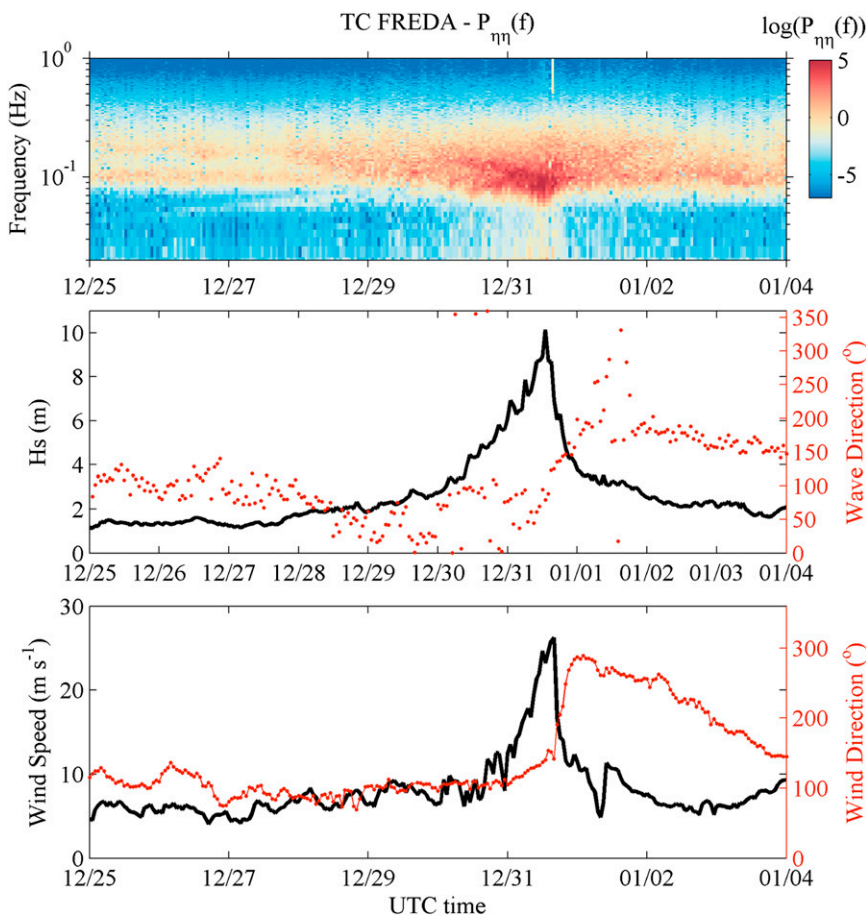


FIG. 6. (top) Spectrogram of the sea surface displacement. Horizontal axis is the time in days. Spectra were computed using 256-s FFT windows with 50% overlap over the 30-min record. (middle) Significant wave height  $H_s$  (black) and wave direction (red, coming from, relative to true north). (bottom) Wind speed measured at 1-m height from the WG (black) and corresponding wind direction (red, coming from, relative to true north).

The Craik–Leibovich II (CLII) theory of Langmuir circulation, or “Langmuir turbulence,” introduces a vortex force that is the vector product of the Stokes drift of the wave field and the vorticity of the Eulerian current,  $\mathbf{F}_v = \mathbf{u}_s \times \boldsymbol{\omega}$ . Early modeling of the effects of the vortex force on the upper ocean used monochromatic wave fields to evaluate the Stokes drift, but recent modeling has used a full directional spectrum (Sullivan et al. 2012) based on Kenyon’s (1969) spectral description of  $\mathbf{u}_s$  as a function of depth. As only directional wave frequency spectra were available in this study, we estimated  $\mathbf{u}_s$  using its leading-order expression derived in Webb and Fox-Kemper (2011):

$$\mathbf{u}_s = \frac{16\pi^3}{g} \int_0^\infty \int_{-\pi}^\pi (\cos\theta, \sin\theta, 0) f^3 S_{f\theta}(f, \theta) e^{(8\pi^2 f^2/g)z} d\theta df, \tag{3}$$

where  $S_{f\theta}$  is the directional wave frequency spectrum,  $z$  is the depth, and  $f$  is the frequency (Hz). Stokes drift

velocity and wind amplitudes and directions are shown in Figs. 10a and 10b. The alignment between Stokes drift velocity and the surface wind is remarkable, reaching at most a 35° offset once the glider is located in the wake of the TC at  $t - t_m = 10$  h, where  $t_m$  is the time when measured winds first reached TC force, at 1200 UTC 31 December 2012 ( $U_{10} = 34.5 \text{ m s}^{-1}$ ).

Figure 10c shows the evolution of the surface turbulent Langmuir number  $La_t$  (McWilliams et al. 1997), defined as

$$La_t = \sqrt{\frac{u_{*w}(t)}{|\mathbf{u}_s(z=0, t)|}}, \tag{4}$$

where  $u_{*w}(t)$  is the friction velocity in the water,  $u_{*w}(t) = \sqrt{|\tau|/\rho_w}$ ,  $\rho_w$  is the water density,  $\tau$  is the surface stress, and  $\mathbf{u}_s(0, t)$  is the surface Stokes drift velocity calculated from (3). Low values of  $La_t$ , below 0.4 in the

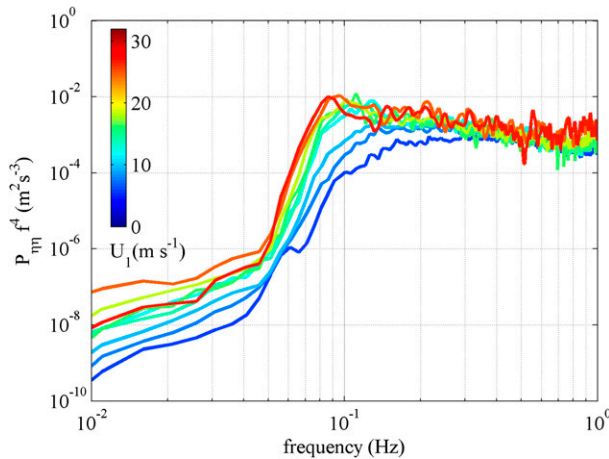


FIG. 7. Evolution of the weighted ( $f^4$ ) wave frequency spectrum as a function of wind speed  $U_1$  (color coded,  $\text{m s}^{-1}$ ) from 1200 UTC 29 Dec 2012 through 1200 UTC 31 Dec 2012. Beyond the peak frequency  $f_p$ , where significant peak enhancement is present, the high-frequency tail of the spectra is approximately proportional to  $f^{-4}$  to  $f^{-5}$  up to 0.7 Hz. Also note the low-frequency swell peak in the low wind case at  $f = 0.06$  Hz.

case of aligned wind and Stokes drift vector, are often associated with the generation of Langmuir circulations. In recent work from [Harcourt and D'Asaro \(2008\)](#), the Langmuir number  $\text{La}_{\text{tsl}}$  (sl stands for surface layer) is defined as  $\text{La}_{\text{tsl}} = \sqrt{u_{*w} / ((u_s)_{\text{sl}} - u_{\text{sref}})}$ , based on a near-surface average value of the Stokes drift  $(u_s)_{\text{sl}}$  and a reference value  $u_{\text{sref}}$  at depth (though still in the mixed layer) to account for vortex force production. The definition of the Langmuir number [see Eq. (4)] was chosen for its simplicity and to provide direct comparison with the numerical simulations of [Sullivan et al. \(2012\)](#). We find the lowest value of  $\text{La}_t$  in front of the storm at  $t = -20$  h and later at  $t = 20$  h, qualitatively consistent with the large eddy simulation (LES) modeling of [Sullivan et al. \(2012\)](#).

The representative vertical penetration of the Stokes drift, the Stokes depth scale (Fig. 10d), is defined by [Sullivan et al. \(2012\)](#) as

$$D_s = 4\pi \int_{z_s}^0 \frac{\mathbf{u}_s(z, t) \cdot \mathbf{u}_s(0, t)}{|\mathbf{u}_s(0, t)|^2} dz, \quad (5)$$

where  $z_s$  is chosen as the depth to which the integrand remains positive.

The Stokes depth scale rapidly increased from 35–45 to up to 126 m over a 40-h period as the storm approached the WG, reaching its maximum at  $t = 4$  h, and then sharply decreased to prestorm levels in only 15 h. Although we do not find a peak in the Stokes depth scale ahead of the storm as shown in [Sullivan et al. \(2012\)](#), we do observe a rapid decrease of  $D_s$  once the glider

reached the rear of the storm, consistent with the analysis of the [Sullivan et al.](#) model TC.

[Figure 11](#) presents the same set of variables ( $\mathbf{u}_s$ ,  $\text{La}_t$ ,  $D_s$ ), this time as a function of position relative to the storm. The axes have been rotated from an Earth-coordinate reference frame to a TC-coordinate reference frame, where the TC is propagating to the left side of the figure. The  $(u_s, v_s)$  vector is rotated in the new reference frame as well for comparison with numerical estimates from [Sullivan et al. \(2012\)](#). The along-track storm direction component of the Stokes drift  $u_s$  is mostly negative in front of the storm, with values reaching up to  $-0.2 \text{ m s}^{-1}$  and then sharply changing sign once the TC wake is reached. The cross-track storm component of the Stokes drift  $v_s$  remains low or close to zero in front of the storm and then reaches a minimum, with a value around  $-0.2 \text{ m s}^{-1}$ , at  $Y = -50$  km and  $X = 70$  km. This asymmetry is explained by the fact that the wind field is less asymmetric than the distribution of the wave field ([Young 2003](#)). The spatial distributions of  $\text{La}_t$  and  $D_s$  are presented in [Figs. 11c and 11d](#). Larger values are found to the right (negative  $Y$ ) side of the TC.

Four profiles of the Stokes velocity at various times and locations with respect to the center of the TC are shown in [Fig. 12](#). The velocity profiles, in a TC-coordinate frame, have been normalized by the local friction velocity in the water, and the depth  $z$  is scaled by  $D_s$ . Recall that the vertical profile of Stokes drift spirals with depth (see [Fig. 13](#)), as it is composed of a mix of swell and wind-wave components, each with an  $e^{kz}$  vertical dependence that propagated in rapidly changing directions as the TC passed near the WG. It is therefore of interest to characterize the depth dependence of the wind–Stokes drift alignment (the included angle between them), as it is directly related to the generation of Langmuir turbulence. [Van Roekel et al. \(2012\)](#) showed that Langmuir turbulence generation is minimal for an included angle of  $180^\circ$  and that the mixing associated with Langmuir circulation is reduced once the included angle reaches  $90^\circ$ .

[Figure 14](#) shows the variation of the wind–Stokes drift included angle as a function of time, for four selected depths ( $z = 0, 10, 40,$  and  $80$  m) along with the magnitude of the wind speed  $U_{10}$  in [Fig. 14a](#) and the evolution of the normalized Stokes drift profile  $(u_s, v_s)/u_{*w}$  as a function of nondimensional depth  $z/D_s$  for the same period of time ([Figs. 14c and 14d](#), respectively). The alignment is generally better at the surface, as shorter locally wind-driven waves rapidly respond to the change in wind direction much faster than it takes for the lower-frequency components of the wave field. Around  $t = -70$  h, as the swell approaches the WG, the misalignment at larger depth (therefore, lower frequency of

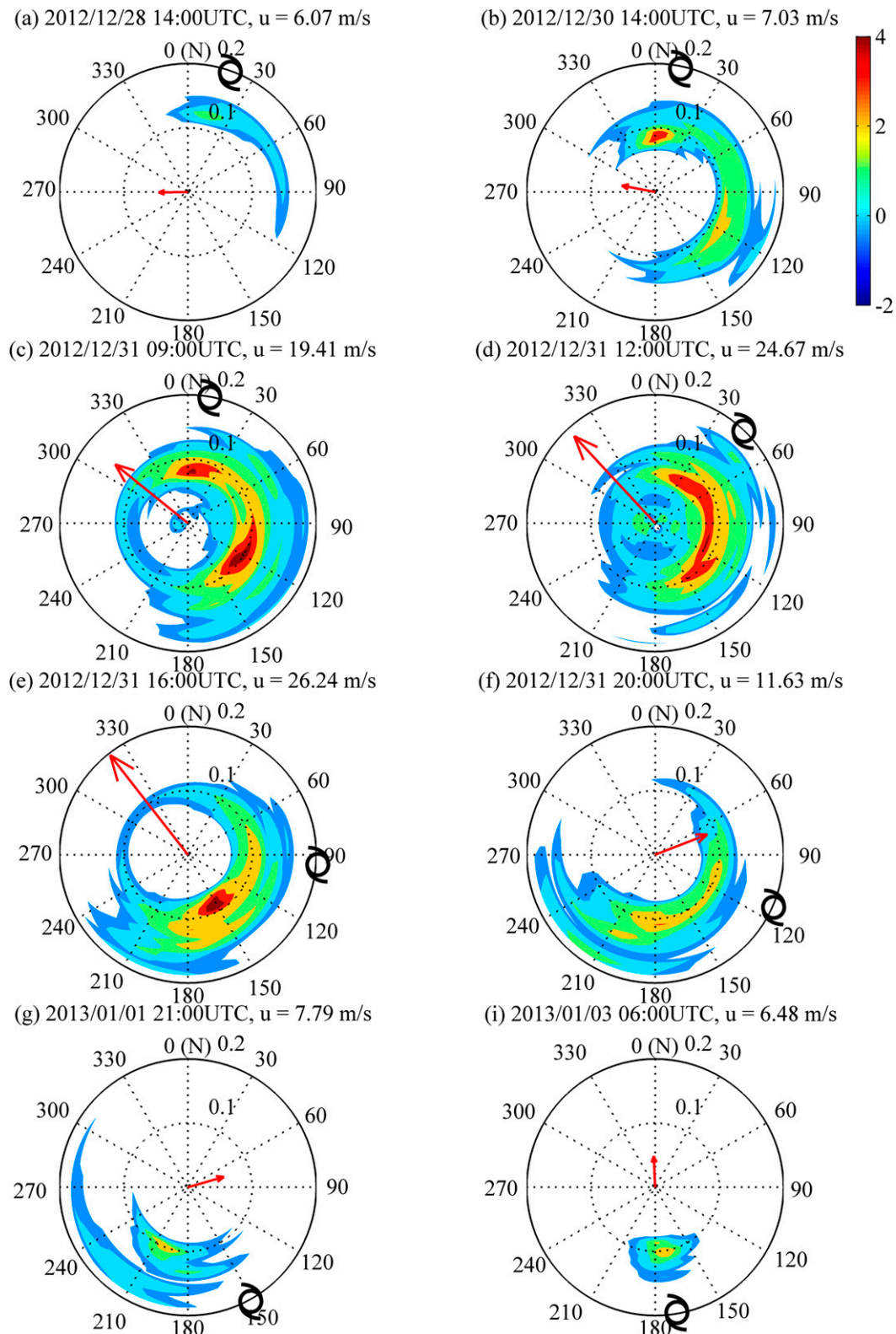


FIG. 8. Evolution of the 30-min wave directional spectrum as TC Freda passed near WG Benjamin. Relative location of the storm is depicted by the TC symbol,  $\odot$ . Wave direction is defined as “coming from,” while the wind vector (red arrow) depicts the direction the wind is “going to,” measured 1 m above the WG float.

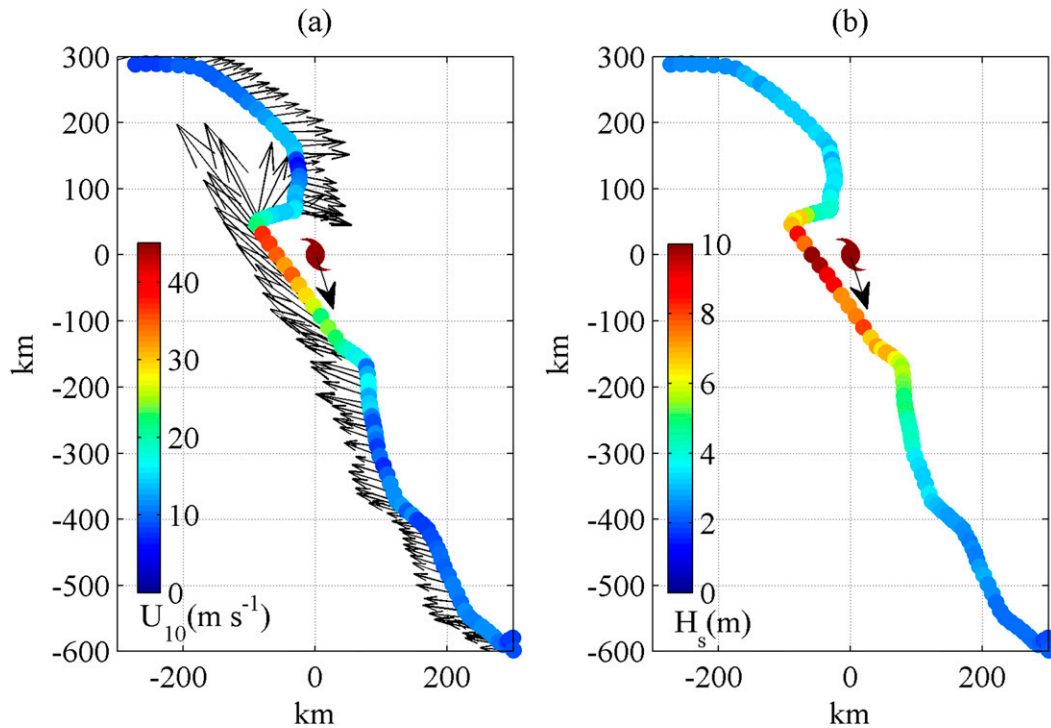


FIG. 9. (a) Wind speed  $U_{10}$  (color coded and shown as vectors along the TC track) and (b)  $H_s$ , as a function of relative distance from the eye of TC Freda. Also shown is the storm mean direction of propagation (black arrow). Both variables are represented as color-coded dots for each record.

the wave field) rapidly increases, reaching almost  $120^\circ$  at  $t = -30$  h. As the glider moves closer to the center of the TC, the surface wave spectrum changes from a multimodal to a unimodal distribution, reducing the depth dependence of the wind–Stokes drift alignment. At  $t = 4$  h, the time of maximum winds, when the wave spectrum is narrow banded (wind waves rapidly aligning to surface forcing), the Stokes drift is in resonance with the wind, meaning that the entire water column, up to the Stokes depth scale, is oriented in, or close to, the wind direction. This is consistent with the results of Sullivan et al. (2012) and of significance, as this implies the generation of strong Langmuir turbulence close to the center of the TC. As the TC propagates away from the Wave Glider, the wind–Stokes drift alignment at depth rapidly deteriorates, briefly reaching  $110^\circ$  at  $t = 10$  h. The alignment subsequently improves over the following 50 h, before wind-wave equilibrium is reached at  $t = 60$  h.

## 5. Biophysical response

Extreme weather events such as tropical cyclones are known to influence nutrient supply and phytoplankton dynamics, providing a mechanism through which cold,

deeper, nutrient-rich water, essential for phytoplankton growth, is entrained into the mixed layer (Babin et al. 2004; Hung et al. 2010; Hung and Gong 2011; Chung et al. 2012; Chen et al. 2013). Conducting traditional ship-based expeditions to collect in situ measurements to characterize the biogeochemical ocean response to such extreme events is difficult (Chen et al. 2013), while satellite observations and estimation of ocean biological productivity variables (e.g., chlorophyll-*a*) are often limited by cloud coverage, especially in close proximity to large weather systems. This is, however, where collocated spatiotemporal measurements of the biological and physical processes are most needed, to characterize the mechanisms through which cold nutrient-rich waters are transported to the surface.

Satellite observations of daily chlorophyll concentration and SST from the Moderate Resolution Imaging Spectroradiometer (MODIS) collected on 25 December 2012 and 3 January 2013 (*before* and *after* the tropical cyclone passage, respectively) are shown in Fig. 15. The track of Freda over the area is shown as a dashed red line, while the location of the storm and the WG on 3 January 2013 is depicted as a red circle and a black cross, respectively, in the two right panels. Despite the limited field of view caused by cloud coverage, especially close

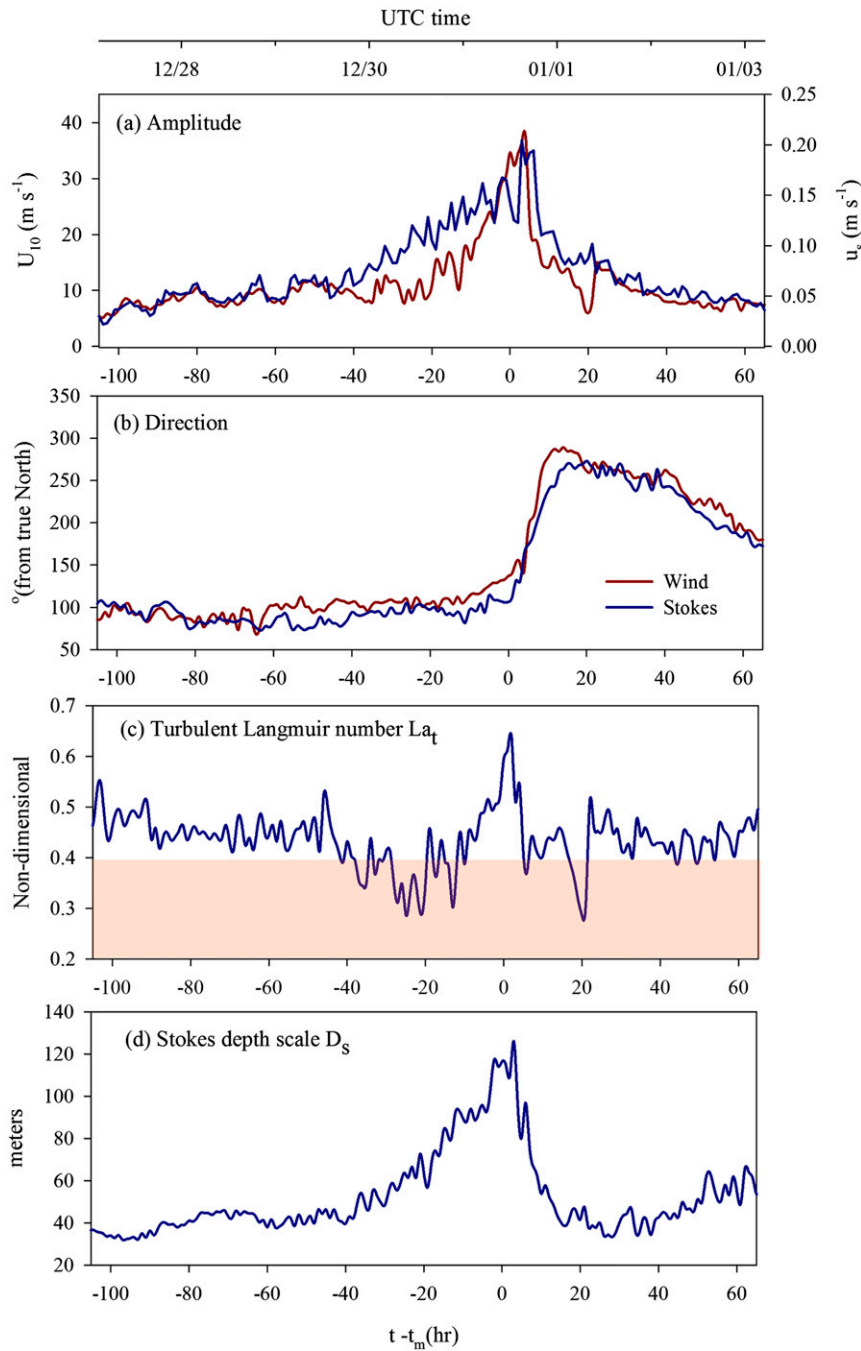


FIG. 10. (a) Amplitude of the surface Stokes drift velocity (blue) and  $U_{10}$  (red) as the WG passed near TC Freda, and (b) corresponding directions. (c) Evolution of the turbulent Langmuir number  $La_t$ , with the colored area corresponding to  $La_t < 0.4$ . (d) Stokes depth scale  $D_s$  for the same period of time.

to the storm, the TC “cold” wake is clearly visible on 3 January 2013, and it exhibits increased concentration of chlorophyll when compared to the prestorm levels, reaching  $0.18 \text{ mg m}^{-3}$  within the wake of the TC. Surface temperature shows a cooling of up to  $4.5^\circ\text{C}$  in response to the TC, even several days after the storm passes.

Chlorophyll-*a* in vivo fluorescence (RFU) is shown in the top panel of Fig. 16. This is not a direct measurement of chl-*a* concentration, as the fluorescence measurements are affected by a range of processes, including photosynthesis and quenching during daytime (Falkowski and Kiefer 1985). The latter explains the large dips in the

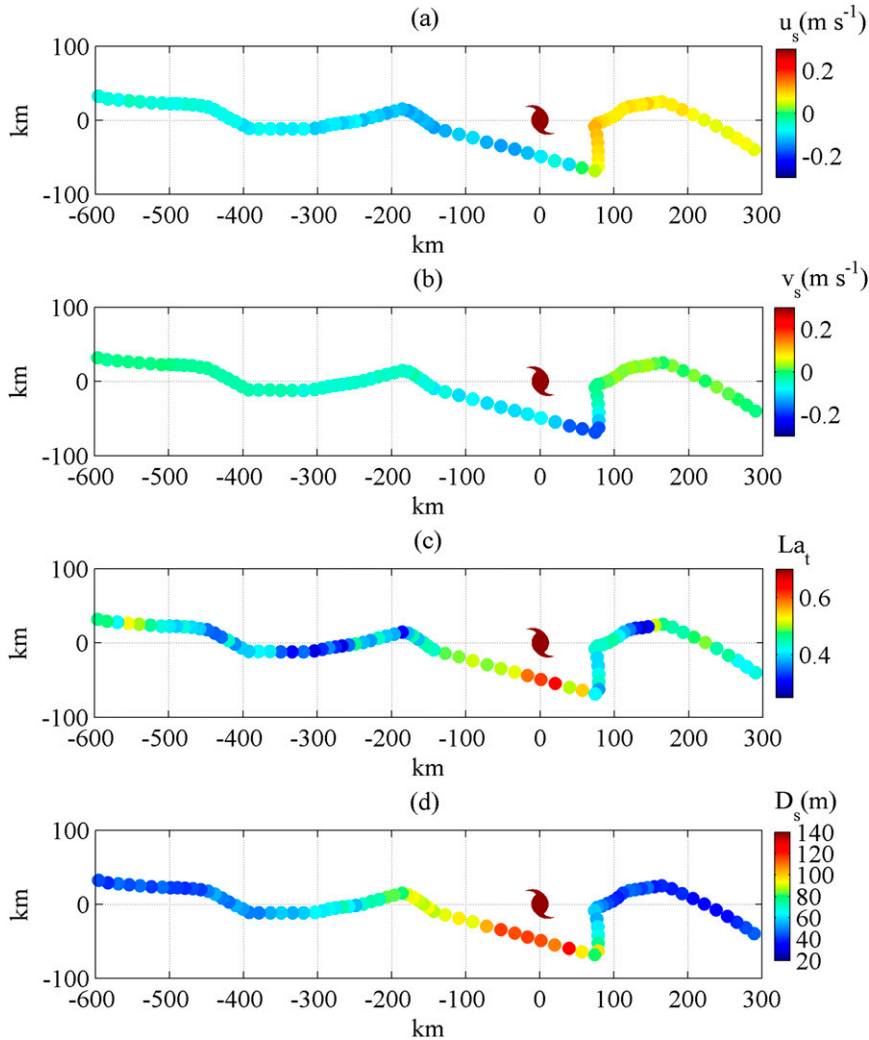


FIG. 11. Along-track and cross-track storm direction components of Stokes drift velocity  $\mathbf{u}_s$  and (b)  $\mathbf{v}_s$ , respectively, calculated at the water surface,  $z = 0$ , from the measured directional wave spectra. (c) Nondimensional turbulent Langmuir number  $La_t$ , and (d) the Stokes depth  $D_s$  (m) as a function of distance from the eye of TC Freda.

chl-*a* fluorescence values during daytime. We chose the nighttime fluorescence data, the period of the day that is least impacted by these processes (highlighted in black in Fig. 16a), as an indicator of the relative evolution of the chl-*a* concentration as the WG passes near the storm. Also shown are the wind speed  $U_{10}$ , significant wave height  $H_s$ , and Wave Glider easterly horizontal velocity (Fig. 16b), SST and surface salinity (Fig. 16c), and dissolved oxygen DO and turbidity (Fig. 16d). The WG easterly horizontal velocity is used as a proxy for the large surface and subsurface currents expected in the wake of the TC (recall from Fig. 3 that the surface current sensor was turned off during the most intense part of the storm). During the studied period, the WG was set to travel toward the west;

therefore, any positive easterly horizontal velocities imply strong surface currents opposing the WG direction of propagation (i.e., the WG is moving backward). The period of time when the WG was located in the wake of the storm, highlighted in blue in Fig. 16, was estimated using the available in situ and satellite products (Fig. 15).

The observed in situ surface temperature fell by  $1.8^\circ\text{C}$  from 30 December 2012 to 2 January 2013, along the track of the WG. The surface salinity drops rapidly starting on 29 December 2012, decreasing to approximately 35.05–35.15 psu for the following 2 days before slowly increasing to 35.3 psu on 4 January 2013. The decrease in salinity is likely due to intense rain close to the storm. Dissolved oxygen concentration rapidly increased as wind speed

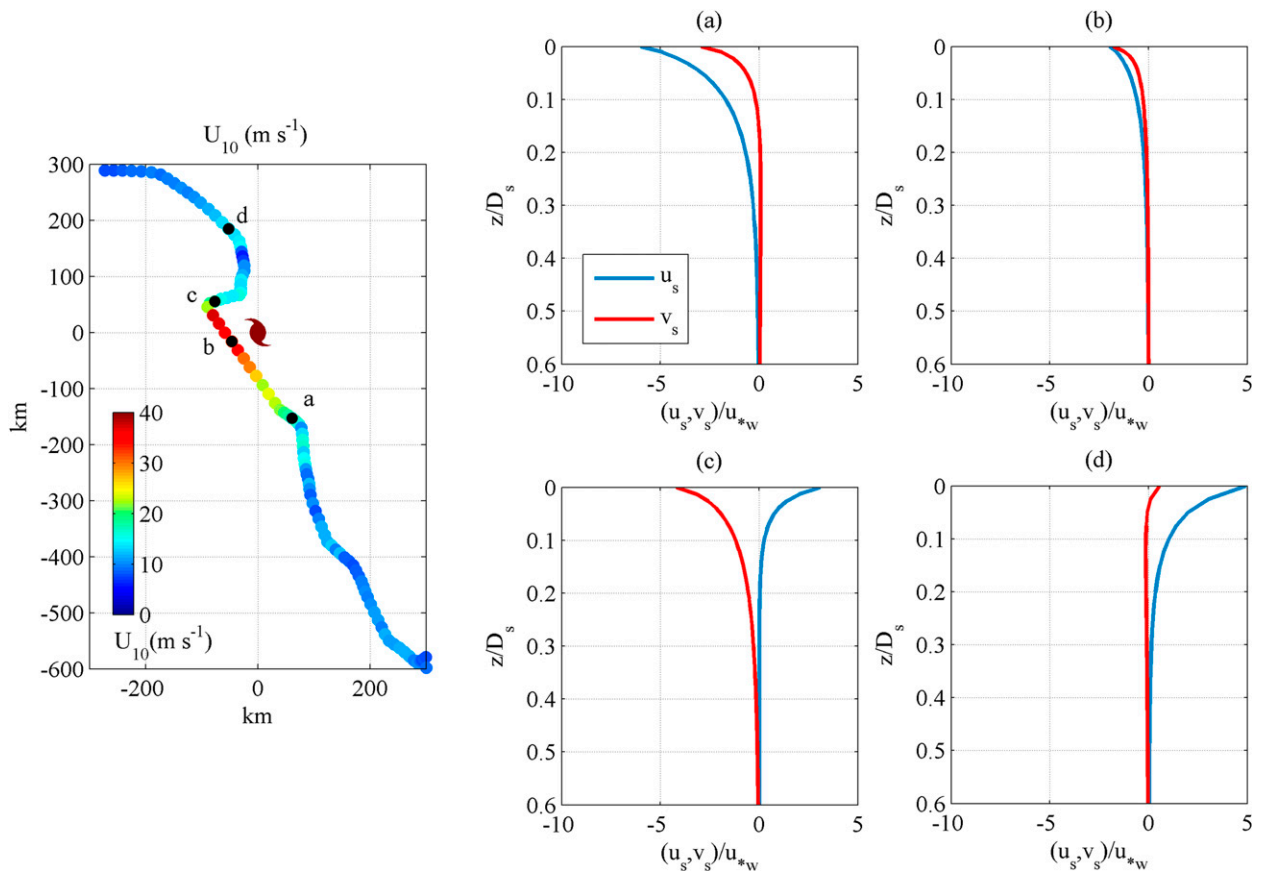


FIG. 12. Vertical profiles of Stokes drift velocity components [along-track and cross-track storm direction components  $u_s$  (blue) and  $v_s$  (red)] normalized by the local friction velocity in the water,  $u_{*w}$ , at (a)–(d) various locations with respect to (left) the eye of the storm. Depth is scaled by  $D_s$ .

rose, caused by the onset of breaking and associated bubble entrainment (Wallace and Wirick 1992; Melville 1996), and then remained at an elevated level for some time.

The observed nighttime chl-*a* in vivo fluorescence increased as the TC passed near the WG, starting from 30 RFU on 28 December 2012 and reaching 50–60 RFU on 31 December 2012. The observed chl-*a* remained at this level (or slightly lower) in the TC wake, and then rapidly reduced to prestorm levels once the WG was out of the TC wake. Although we do expect a bias in the chl-*a* fluorescence caused by bubble contamination in the optical measurements (Terrill et al. 2001; Omand et al. 2009), this would not account for the significant rise of chl-*a* fluorescence occurring between 29 December 2012 and 31 December 2012. In addition, the turbidity measurements shown in Fig. 16d only exhibit a significant increase, also known to be associated with subsurface bubble generation, at the peak of the storm. Note that the apparent constant chl-*a* in vivo fluorescence in the TC

wake from 31 December 2012 to 1 January 2013 whereas the SST keeps decreasing suggests that all nutrient-rich water from the euphotic layer was entrained into the mixed layer.

## 6. Summary and discussion

Atmospheric and oceanographic measurements collected during Tropical Cyclone Freda from an instrumented surface vehicle have been analyzed. The Wave Glider was able to withstand TC (hurricane)-level wind and wave conditions while collecting and transmitting measurements.

The standard surface ocean–lower atmosphere (SOLA) measurements of air temperature, winds, SST, and surface currents were measured. In addition, using the motion of the surface flotation for wave field measurements calibrated against a standard wave buoy, the evolution of the directional wave field as the storm passed near the WG was measured and analyzed. It exhibited a transition from

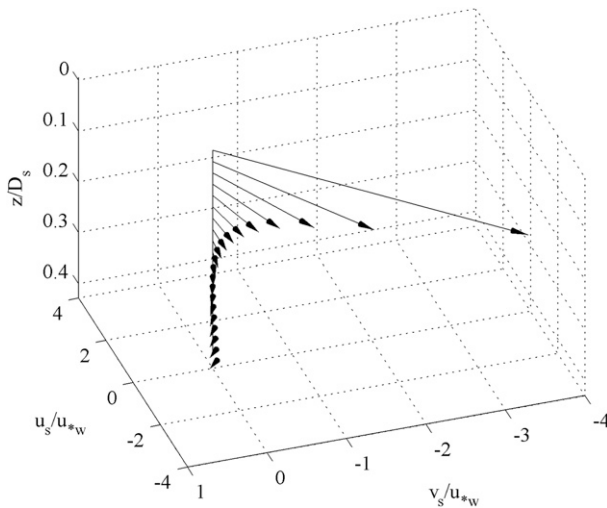


FIG. 13. Example of vertical profiles of Stokes drift velocity normalized by  $u_{*w}$  at 0200 UTC 31 Dec 2012. Depth is scaled by  $D_s$ .

a unimodal (swell) to a bimodal distribution (swell plus wind waves) in front of the TC, changing to a unimodal distribution close to the eye of the TC and in its wake. The frequency spectrum of the sea surface displacement (i.e., the wave spectrum) shows close to an  $f^{-4}$  dependency over a range of frequencies, consistent with past studies (Donelan et al. 1985; Young 2006).

Stokes drift velocities were estimated from the wave directional spectrum. The Langmuir turbulence number, the Stokes depth scale, and the Stokes drift computed from measurements of the directional wave spectrum across the track of TC Freda show remarkable agreement with recent hurricane marine boundary layer studies that include numerical wind-wave model predictions as input into the LES model of the marine boundary layer (Sullivan et al. 2012). The surface turbulent Langmuir number  $La_t$ , based on wave measurements, varied from 0.28 to 0.6, with the lower values, below 0.4, found ahead of the storm and in its wake. We find a spatial distribution of the Stokes drift vector comparable to that in Sullivan et al. (2012), with a maximum magnitude at the closest point from the eye of the TC, to its right side, mostly driven by  $v_s$ , the component orthogonal to the path of the TC. Though we do expect an enhancement of vertical mixing by Langmuir turbulence through the vortex force when the Stokes drift vector is aligned with the current, large misalignments between the wind and Stokes drift vector, at depth in particular, will lead to situations where the vertical gradients of Eulerian velocities and Stokes drift are of opposing signs, effectively reducing the contribution of Langmuir turbulence to vertical mixing. This is of importance, as the depth penetration of the Stokes drift,

characterized as the Stokes depth scale, was found to exceed 120 m at the time of maximum winds.

Although the deepening of the mixed layer produced by the wake of inertial currents formed behind a tropical cyclone or hurricane (e.g., Price 1981) remains the dominant dynamical process through which cold, deeper water is entrained into the mixed layer in the wake of TCs and hurricanes, this does not explain the apparent entrainment or upwelling ahead of Freda demonstrated by the chl-*a* data presented here. It appears that other mechanisms may need to be considered.

Toffoli et al. (2012) suggest wave-orbital-motion-induced turbulence as a possible process to explain the deepening of the mixed layer during tropical cyclones; however, evidence for such turbulence is based on very limited indirect laboratory studies, and as far as we are aware there is no direct field evidence of such turbulence. Recent numerical studies from Sullivan et al. (2012) show the importance of Langmuir turbulence, which is estimated to contribute up to 20% of the entrainment flux at the base of a marine boundary layer driven by a hurricane. Turbulence generated by wave breaking, a dominant feature of such high wind and wave environments, was not taken into account in this study, but it may contribute significantly (Sullivan et al. 2007) to ocean mixing, through direct injection of turbulence near the surface, which is transported to deeper water by Langmuir circulations. We expect this latter process to be important in tropical cyclones, in particular ahead of the storm, where the Stokes depth scale can reach very large values (up to 120 m for TC Freda).

Another mechanism to consider is the Ekman pumping  $w_E$ , defined as

$$w_E = \frac{\mathbf{V} \times \boldsymbol{\tau}}{\rho_w f_c}, \quad (6)$$

where  $\mathbf{V} \times \boldsymbol{\tau}$  is the wind stress curl and  $f_c$  is the Coriolis parameter. Figure 16e shows  $w_E$  calculated from the JTWC/W3 product (gray line) at the WG location. The upwelling velocity reached  $5.5 \text{ m h}^{-1}$  at the peak of the storm, in an area where the winds were very high ( $U_{10} > 25 \text{ m s}^{-1}$ ) and their direction was rapidly changing. Also shown is the vertical velocity generated from the spatial divergence of horizontal Stokes drift, introduced by McWilliams et al. (2004) as a pseudovertical velocity  $w^{\text{St}}$  (red line). This velocity does contribute to the vertical transport near the most intense part of the TC, though to a lesser degree than the Ekman pumping.

Future versions of the SOLA-instrumented Wave Glider should include a current profiler to estimate the Eulerian current shear, which is an important source of mixing in the wake of tropical cyclones, as well as the

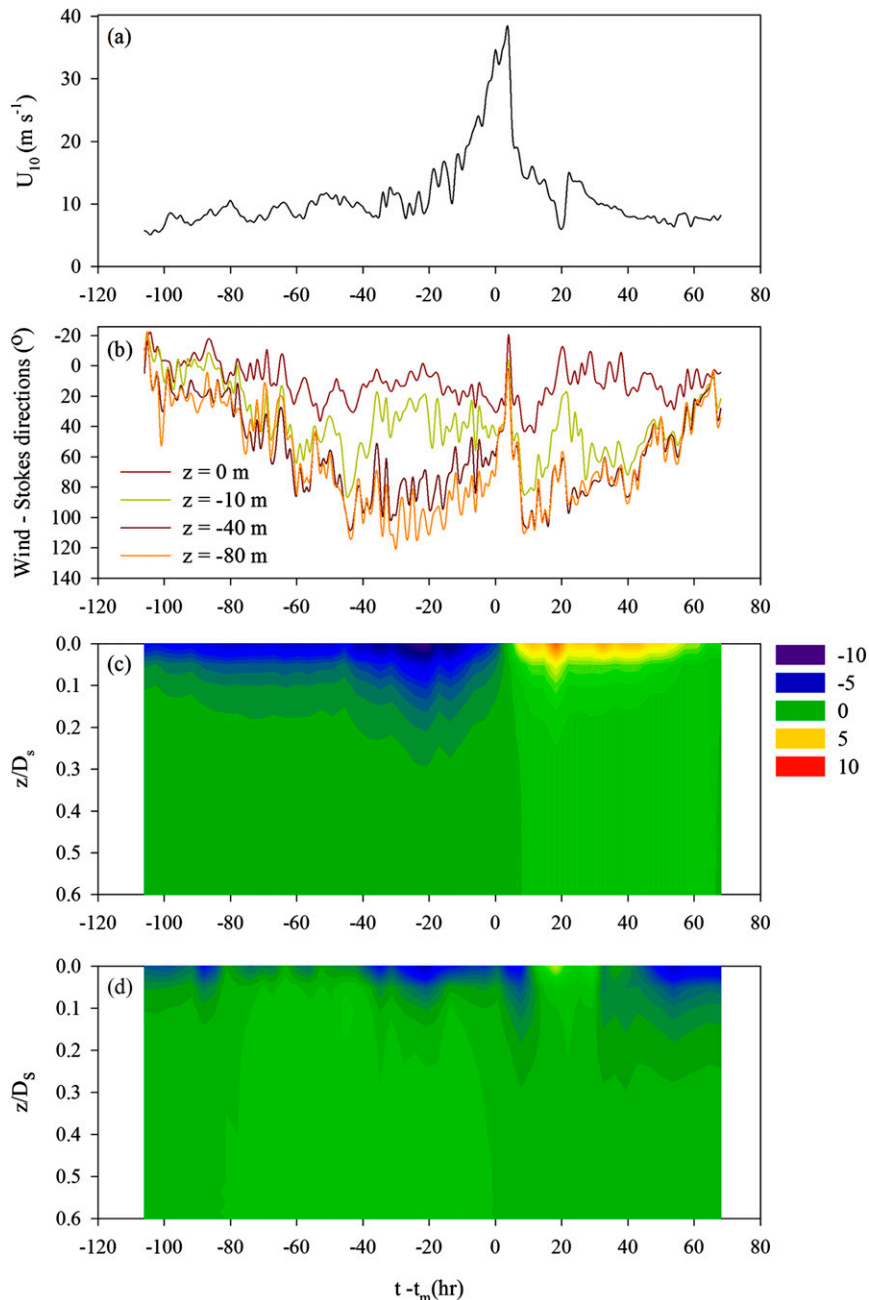


FIG. 14. (a) Wind speed  $U_{10}$  as the WG passed near TC Freda. (b) Difference between the direction of the mean wind and that of the Stokes drift  $u_s(z)$  for  $z = 0, -10, -40, -80$  m, as a function of time relative to maximum wind. (c),(d) Color-coded vertical profiles of Stokes drift  $(u_s, v_s)$  normalized by  $u_{w*}$  as a function of nondimensional depth  $z/D_s$ , respectively.

Stokes shear-production term as a function of depth in the nonequilibrium wind-wave regime.

One of the most important conclusions of this work is that the SOLA measurements, made in close proximity to a category 3 tropical cyclone using the Wave Glider, make way for more extensive use of this technology in

measuring air-sea interaction processes in extreme conditions. There is room for improvement in using more research-grade instrumentation to measure SOLA processes. There is also the opportunity to park a small flotilla of these platforms in “hurricane alley” locations and, with a 5–7-day hurricane forecast window, be able

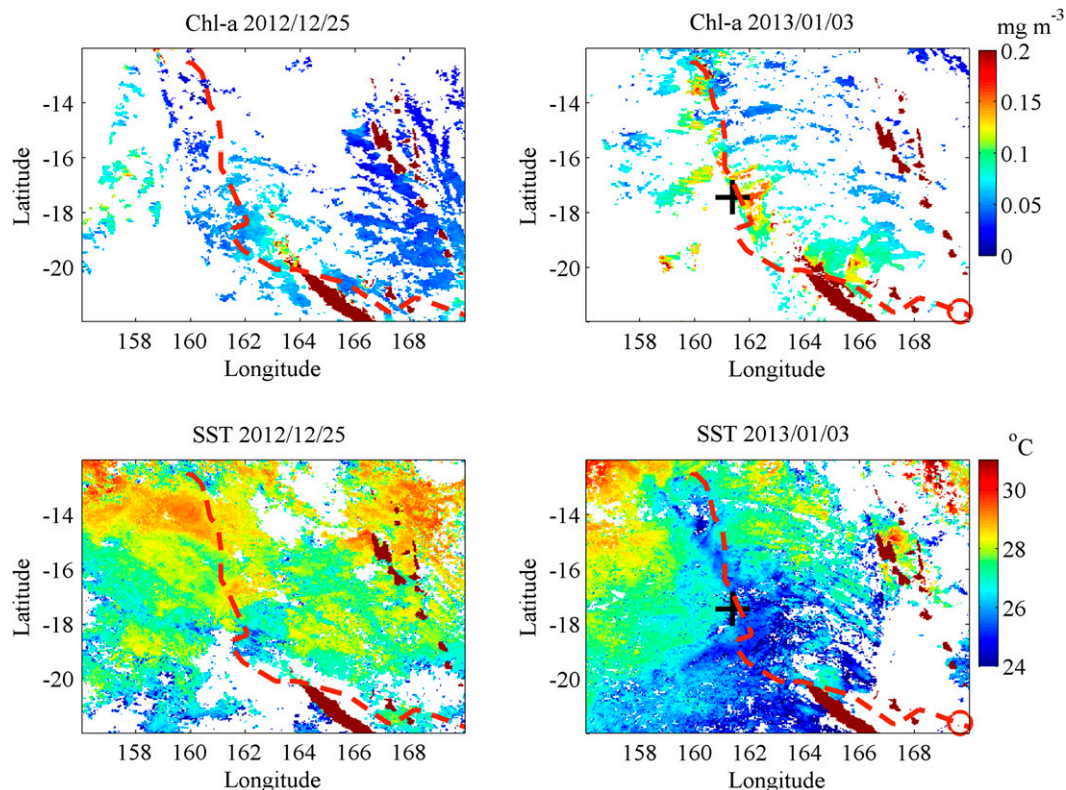


FIG. 15. (top) Chl-*a* concentration estimated from MODIS and *Terra* level 3 daily products ( $\text{mg m}^{-3}$ ) (left) before and (right) after TC Freda. Track of the TC is shown as a red dashed line. Average location of the center of the storm and the WG on 3 Jan 2013 are depicted by a red circle and a black cross, respectively. (bottom) Corresponding SST.

to send them to cross the hurricane track at various locations.

*Acknowledgments.* The authors thank Liquid Robotics, Sunnyvale, California, for supplying the PacX dataset; Jesse Thomas and Roger Hine (Liquid Robotics) for assisting with data formats and valuable discussions; John Knaff (NOAA) for providing the RAMMB dataset; and Buck Sampson (NRL) for supplying the TC Freda JTWC/W3 product. This research was supported by funding to WKM from the Office of Naval Research HiRes DRI (Physical Oceanography), from an ONR DURIP award for our current development of SOLA-instrumented Wave Gliders, and from NSF (Physical Oceanography).

## APPENDIX

### Directional Wave Measurements from a Wave Glider

While the Wave Glider is equipped with a Datawell directional wave sensor, the Wave Glider platform is

not optimized for wave measurement as is the Datawell family of wave buoys, so a direct intercomparison of wave measurements from the two platforms was conducted.

A short deployment of Wave Glider *Benjamin* to evaluate its performance as a directional wave sensor was conducted by Liquid Robotics prior to the start of the PacX project, from 0400 UTC 8 December 2011 to 0200 UTC 10 December 2011, in close proximity to a Mark II Datawell directional wave buoy [Coastal Data Information Program (CDIP) 156] located in Monterey Bay, California. Figure A1a shows the glider track, relative to the buoy location. Two polygonal patterns centered on the buoy location were used: a larger one, with sides of approximately 1.3 km, and a smaller one, with sides of approximately 300–400 m in length. The Datawell buoy is sampled at 1.28 Hz, with a low-frequency cutoff at 0.033 Hz, while the Wave Glider DWR-G is sampled at 2 Hz with a cutoff at 0.01 Hz. Horizontal ( $x$ ,  $y$ ) and vertical ( $z$ ) displacements of the buoy and Wave Glider were analyzed to compute bulk wave parameters shown in Figs. A1b–d. For each 30-min record, autospectra, cospectra, and quadrature

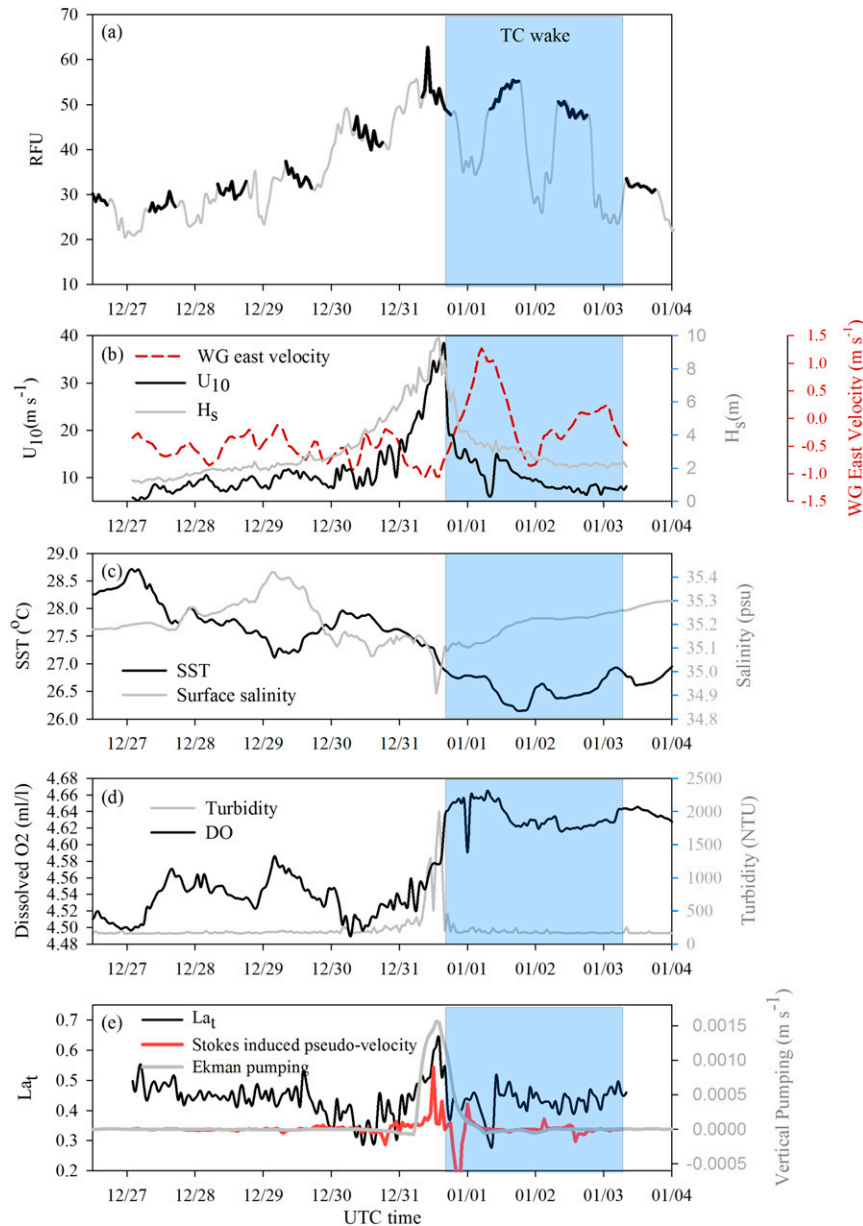


FIG. 16. Ocean surface conditions measured by WG during TC Freda. (a) Chl-*a* in vivo fluorescence, where the bold black lines represent the nighttime portion of the dataset; (b) significant wave height ( $H_s$ ; gray), wind speed  $U_{10}$  ( $\text{m s}^{-1}$ ; black), and horizontal easterly WG velocity ( $\text{m s}^{-1}$ ; red); (c) SST and surface salinity; (d) dissolved oxygen (DO) and turbidity; and (e) Langmuir number, Stokes induced pseudo-velocity  $w^{\text{St}}$ , and Ekman pumping  $w_E$ .

spectra were computed using 256-s FFT windows with a 50% overlap. Significant wave height  $H_s$  was computed as  $H_s = 4\langle\eta^2\rangle$ , where  $\eta(t)$  is the vertical displacement and  $\langle\cdot\rangle$  is the time average; the peak period  $T_p$  as the most energetic frequency in a given wave spectrum; and  $D_p$  as the corresponding peak direction.

Overall, the bulk parameters estimated from the Wave Glider and the Datawell directional wave buoy are in very good agreement. In addition, standard methods are used to compute frequency-dependent mean wave direction  $\bar{\theta}(f)$  and directional spread  $\sigma_\theta(f)$ , based on the first- and second-order Fourier moments of the

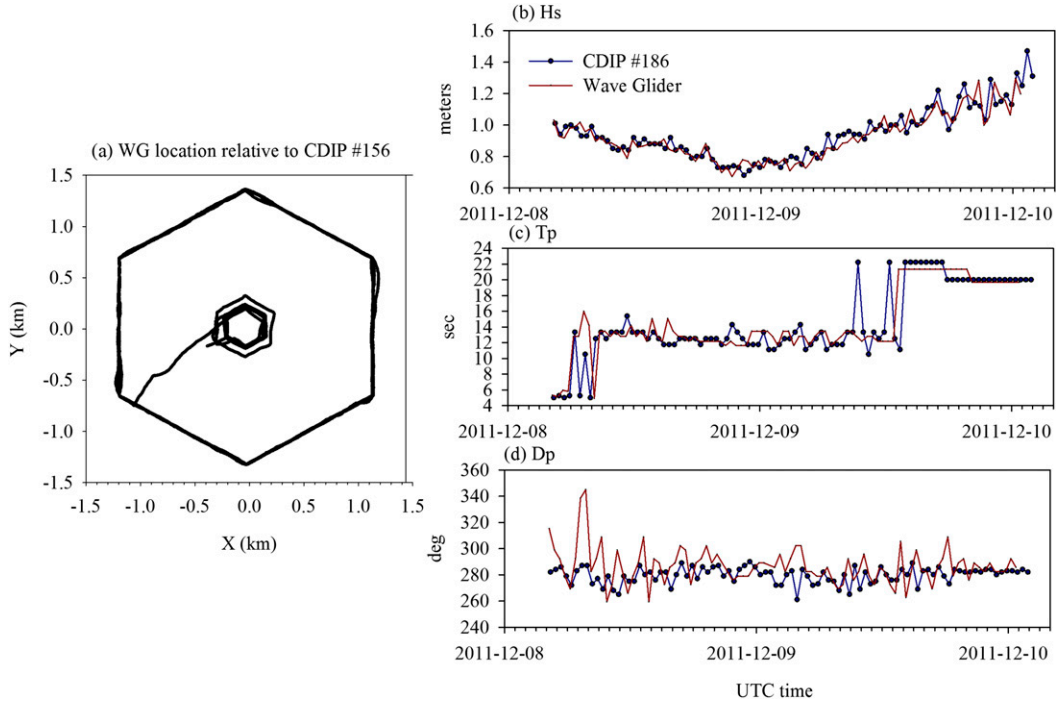


FIG. A1. (a) WG position relative to CDIP buoy 156 from 0400 UTC 8 Dec 2011 to 0200 UTC 10 Dec 2011. (right) Comparison of bulk parameters between the WG measurements and the wave buoy for the same period of time: (a)  $H_s$ , (b)  $T_p$ , and (c)  $D_p$  (coming from, true north).

directional distribution of wave energy  $S(\theta)$ , expressed in terms of autospectra ( $E_{xx}, E_{yy}, E_{zz}$ ), cospectra ( $C_{xy}$ ), and quadrature ( $Q_{xz}, Q_{yz}$ ) spectra (Long 1980; Herbers et al. 2012). In this study, the mean direction  $\bar{\theta}$  and directional spread  $\sigma_\theta$  were computed using the first-order moments  $a_1$  and  $b_1$  of the directional distribution:

$$\tan(\bar{\theta}) = \frac{b_1}{a_1} \tag{A1}$$

and

$$\sigma_\theta = \sqrt{2(1 - \sqrt{a_1^2 + b_1^2})}, \tag{A2}$$

where

$$\begin{pmatrix} a_1 \\ b_1 \\ a_2 \\ b_2 \end{pmatrix} = \begin{bmatrix} Q_{xx}/\sqrt{(E_{xx} + E_{yy})E_{zz}} \\ Q_{yz}/\sqrt{(E_{xx} + E_{yy})E_{zz}} \\ (E_{xx} - E_{yy})/(E_{xx} + E_{yy}) \\ 2C_{xy}/(E_{xx} + E_{yy}) \end{bmatrix}. \tag{A3}$$

A representative sample from the Wave Glider (dark red) and Datawell directional wave buoy (dark blue) is shown in Fig. A2. Figure A2a shows the wave frequency spectrum, Fig. A2b the mean wave direction, and Fig. A2c the directional spread. The wave field is dominated by swell coming from the west, and wind waves were also coming from the west while a higher frequency component coming from the east was also observed. The agreement in wave spectral estimates is excellent for frequencies ranging from 0.033 to 0.64 Hz, the spectral range of the Datawell directional buoy sensor. The mean wave directions computed from the Wave Glider measurements are in good agreement with those of the Datawell buoy, though noisier, especially at lower frequencies. The directional spread estimated from the Wave Glider is larger for the lower frequencies.

From these comparisons, it appears that the quality of the wave directional data measured from the Wave Glider is comparable to that from the standard Datawell directional wave buoy, with the exception of signal-to-noise ratios and directional spreading at lower frequencies. It is likely that these differences at lower frequencies are due to the differences between the tether design optimized for wave measurements by the

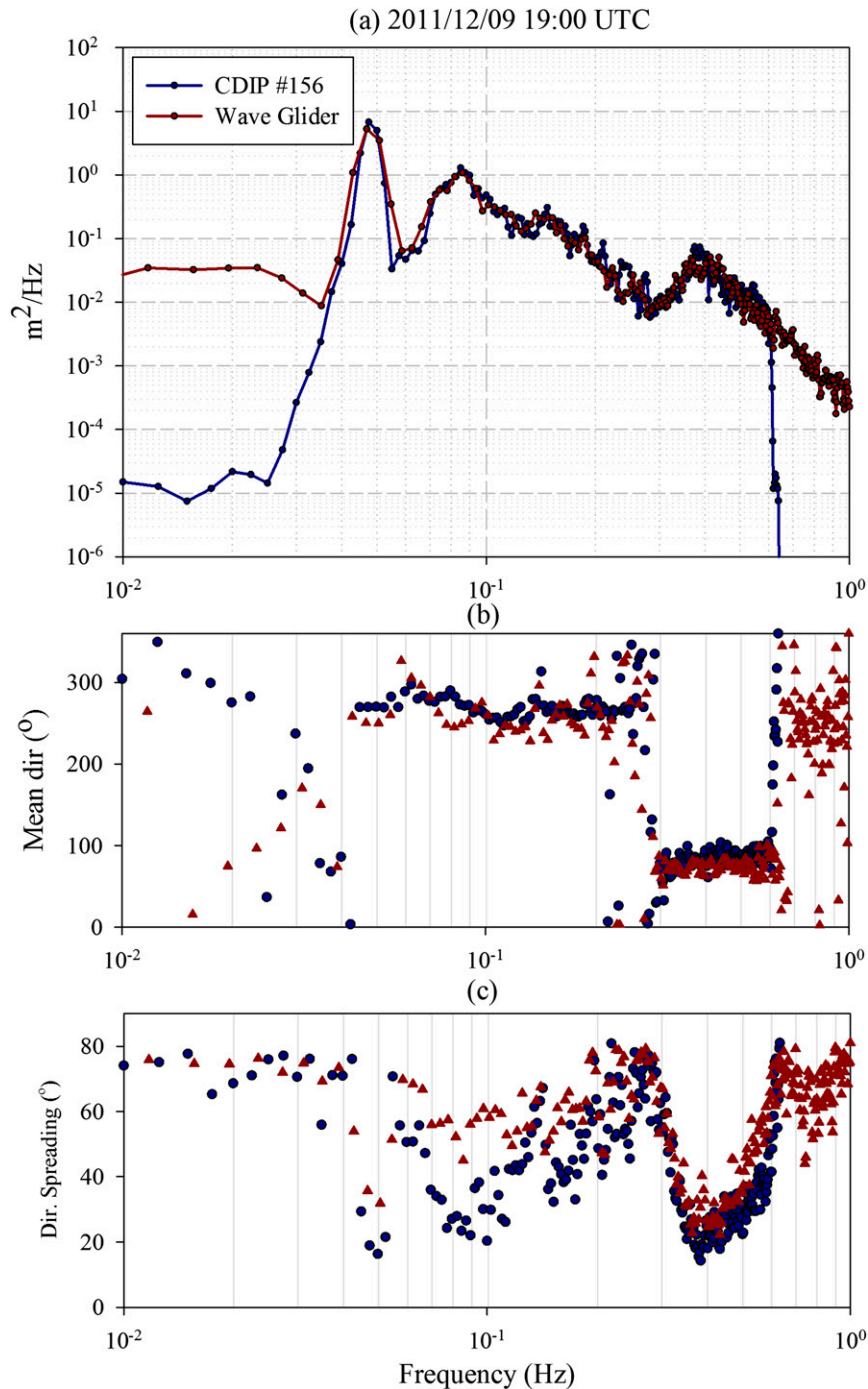


FIG. A2. Example comparison of (a) wave frequency spectra computed from 30 min of data collected at 1900 UTC 9 Dec 2011, (b) frequency-dependent mean direction  $\bar{\theta}(f)$  and (c) directional spread  $\sigma_\theta(f)$ .

buoy, and the constraints of the tether on the Wave Glider, which is optimized for propulsion. Notwithstanding these low-frequency differences, the measurements demonstrate that the Wave Glider is a useful directional wave measurement platform.

#### REFERENCES

- Babin, S. M., J. A. Carton, T. D. Dickey, and J. D. Wiggert, 2004: Satellite evidence of hurricane-induced phytoplankton blooms in an oceanic desert. *J. Geophys. Res.*, **109**, C03043, doi:10.1029/2003JC001938.

- Bell, M. M., M. T. Montgomery, and K. A. Emanuel, 2012: Air-sea enthalpy and momentum exchange at major hurricane wind speeds observed during CBLAST. *J. Atmos. Sci.*, **69**, 3197–3222, doi:10.1175/JAS-D-11-0276.1.
- Bender, M. A., I. Ginis, R. Tuleya, B. Thomas, and T. Marchok, 2007: The operational GFDL coupled hurricane–ocean prediction system and a summary of its performance. *Mon. Wea. Rev.*, **135**, 3965–3989, doi:10.1175/2007MWR2032.1.
- Black, P. G., and Coauthors, 2007: Air–sea exchange in hurricanes: Synthesis of observations from the coupled boundary layer air–sea transfer experiment. *Bull. Amer. Meteor. Soc.*, **88**, 357–374, doi:10.1175/BAMS-88-3-357.
- Brodtkorb, P. A., P. Johannesson, G. Lindgren, I. Rychlik, J. Rydén, and E. Sjö, 2000: WAFO: A Matlab toolbox for analysis of random waves and loads. *Proc. 10th Int. Offshore and Polar Engineering Conf.*, Vol III, Seattle, WA, ISOPE, 343–350.
- Charnock, H., J. R. D. Francis, P. A. Sheppard, F. Pasquill, R. J. Murgatroyd, and J. Malkus, 1955: Medium-scale turbulence in the trade winds. *Quart. J. Roy. Meteor. Soc.*, **81**, 634–635, doi:10.1002/qj.49708135022.
- Chen, K.-S., C.-C. Hung, G.-C. Gong, W.-C. Chou, C.-C. Chung, Y.-Y. Shih, and C.-C. Wang, 2013: Enhanced POC export in the oligotrophic northwest Pacific Ocean after extreme weather events. *Geophys. Res. Lett.*, **40**, 5728–5734, doi:10.1002/2013GL058300.
- Chung, C.-C., G.-C. Gong, and C.-C. Hung, 2012: Effect of Typhoon Morakot on microphytoplankton population dynamics in the subtropical northwest Pacific. *Mar. Ecol. Prog. Ser.*, **448**, 39–49, doi:10.3354/meps09490.
- Craik, A. D. D., and S. Leibovich, 1976: A rational model for Langmuir circulations. *J. Fluid Mech.*, **73**, 401–426, doi:10.1017/S0022112076001420.
- D’Asaro, E. A., R. Harcourt, E. Terrill, P. P. Niiler, and T. B. Sanford, 2006: The hurricane mixing front. *Bull. Amer. Meteor. Soc.*, **87**, 1492–1492.
- , T. B. Sanford, P. P. Niiler, and E. J. Terrill, 2007: Cold wake of Hurricane Frances. *Geophys. Res. Lett.*, **34**, L15609, doi:10.1029/2007GL030160.
- Donelan, M. A., J. Hamilton, and W. H. Hui, 1985: Directional spectra of wind-generated waves. *Philos. Trans. Roy. Soc. London*, **315A**, 509–562, doi:10.1098/rsta.1985.0054.
- Fairall, C. W., E. F. Bradley, J. E. Hare, A. A. Grachev, and J. B. Edson, 2003: Bulk parameterization of air–sea fluxes: Updates and verification for the COARE algorithm. *J. Climate*, **16**, 571–591, doi:10.1175/1520-0442(2003)016<0571:BPOASF>2.0.CO;2.
- Falkowski, P., and D. A. Kiefer, 1985: Chlorophyll *a* fluorescence in phytoplankton: Relationship to photosynthesis and biomass. *J. Plankton Res.*, **7**, 715–731, doi:10.1093/plankt/7.5.715.
- Harcourt, R. R., and E. A. D’Asaro, 2008: Large-eddy simulation of Langmuir turbulence in pure wind seas. *J. Phys. Oceanogr.*, **38**, 1542–1562, doi:10.1175/2007JPO3842.1.
- Herbers, T. H. C., P. F. Jessen, T. T. Janssen, D. B. Colbert, and J. H. MacMahan, 2012: Observing ocean surface waves with GPS-tracked buoys. *J. Atmos. Oceanic Technol.*, **29**, 944–959, doi:10.1175/JTECH-D-11-00128.1.
- Hung, C.-C., and G. C. Gong, 2011: Biogeochemical responses in the southern East China Sea after typhoons. *Oceanography*, **24**, 42–51, doi:10.5670/oceanog.2011.93.
- , and Coauthors, 2010: The effect of typhoon on particulate organic carbon flux in the southern East China Sea. *Biogeochemistry*, **7**, 3007–3018, doi:10.5194/bg-7-3007-2010.
- Kenyon, K. E., 1969: Stokes drift for random gravity waves. *J. Geophys. Res.*, **74**, 6991–6994, doi:10.1029/JC074i028p06991.
- Knaff, J. A., M. DeMaria, D. A. Molenaar, C. R. Sampson, and M. G. Seybold, 2011: An automated, objective, multiple-satellite-platform tropical cyclone surface wind analysis. *J. Appl. Meteor. Climatol.*, **50**, 2149–2166, doi:10.1175/2011JAMC2673.1.
- , —, C. R. Sampson, J. E. Peak, J. Cummings, and W. H. Schubert, 2013: Upper oceanic energy response to tropical cyclone passage. *J. Climate*, **26**, 2631–2650, doi:10.1175/JCLI-D-12-00038.1.
- Lamarre, E., and W. K. Melville, 1991: Air entrainment and dissipation in breaking waves. *Nature*, **351**, 469–472, doi:10.1038/351469a0.
- Long, R. B., 1980: The statistical evaluation of directional spectrum estimates derived from pitch-roll buoy data. *J. Phys. Oceanogr.*, **10**, 944–952, doi:10.1175/1520-0485(1980)010<0944:TSEODS>2.0.CO;2.
- McWilliams, J. C., P. P. Sullivan, and C. H. Moeng, 1997: Langmuir turbulence in the ocean. *J. Fluid Mech.*, **334**, 1–30, doi:10.1017/S0022112096004375.
- , J. M. Restrepo, and E. M. Lane, 2004: An asymptotic theory for the interaction of waves and currents in coastal waters. *J. Fluid Mech.*, **511**, 135–178, doi:10.1017/S0022112004009358.
- Melville, W. K., 1996: The role of surface-wave breaking in air–sea interaction. *Annu. Rev. Fluid Mech.*, **28**, 279, doi:10.1146/annurev.fl.28.010196.001431.
- Moon, I. J., I. Ginis, T. Hara, H. L. Tolman, C. W. Wright, and E. J. Walsh, 2003: Numerical simulation of sea surface directional wave spectra under hurricane wind forcing. *J. Phys. Oceanogr.*, **33**, 1680–1706, doi:10.1175/2410.1.
- Mrvljajevic, R. K., and Coauthors, 2013: Observations of the cold wake of Typhoon Fanapi (2010). *Geophys. Res. Lett.*, **40**, 316–321, doi:10.1029/2012GL054282.
- Omand, M. M., F. Feddersen, D. B. Clark, P. J. S. Franks, J. J. Leichter, and R. T. Guza, 2009: Influence of bubbles and sand on chlorophyll-*a* fluorescence measurements in the surfzone. *Limnol. Oceanogr. Methods*, **7**, 354–362, doi:10.4319/lom.2009.7.354.
- Powell, M. D., P. J. Vickery, and T. A. Reinhold, 2003: Reduced drag coefficient for high wind speeds in tropical cyclones. *Nature*, **422**, 279–283, doi:10.1038/nature01481.
- Price, J. F., 1981: Upper ocean response to a hurricane. *J. Phys. Oceanogr.*, **11**, 153–175, doi:10.1175/1520-0485(1981)011<0153:UORTAH>2.0.CO;2.
- Sampson, C. R., P. A. Wittmann, and H. L. Tolman, 2010: Consistent tropical cyclone wind and wave forecasts for the U.S. Navy. *Wea. Forecasting*, **25**, 1293–1306, doi:10.1175/2010WAF2222376.1.
- , —, E. A. Serra, H. L. Tolman, J. Schauer, and T. Marchok, 2013: Evaluation of wave forecasts consistent with tropical cyclone warning center wind forecasts. *Wea. Forecasting*, **28**, 287–294, doi:10.1175/WAF-D-12-00060.1.
- Sanford, T. B., J. F. Price, J. B. Girton, and D. C. Webb, 2007: Highly resolved observations and simulations of the ocean response to a hurricane. *Geophys. Res. Lett.*, **34**, L13604, doi:10.1029/2007GL029679.
- , K. A. Kelly, and D. M. Farmer, 2011a: Sensing the ocean. *Phys. Today*, **64**, 24–28, doi:10.1063/1.3554313.
- , J. F. Price, and J. B. Girton, 2011b: Upper-ocean response to Hurricane Frances (2004) observed by profiling EM-APEX floats. *J. Phys. Oceanogr.*, **41**, 1041–1056, doi:10.1175/2010JPO4313.1.
- Sullivan, P. P., and J. C. McWilliams, 2010: Dynamics of winds and currents coupled to surface waves. *Annu. Rev. Fluid Mech.*, **42**, 19–42, doi:10.1146/annurev-fluid-121108-145541.

- , —, and W. K. Melville, 2007: Surface gravity wave effects in the oceanic boundary layer: Large-eddy simulation with vortex force and stochastic breakers. *J. Fluid Mech.*, **593**, 405–452, doi:10.1017/S002211200700897X.
- , L. Romero, J. C. McWilliams, and W. K. Melville, 2012: Transient evolution of Langmuir turbulence in ocean boundary layers driven by hurricane winds and waves. *J. Phys. Oceanogr.*, **42**, 1959–1980, doi:10.1175/JPO-D-12-025.1.
- Terrill, E. J., W. K. Melville, and D. Stramski, 2001: Bubble entrainment by breaking waves and their influence on optical scattering in the upper ocean. *J. Geophys. Res.*, **106**, 16815–16823, doi:10.1029/2000JC000496.
- Toffoli, A., J. McConochie, M. Ghantous, L. Loffredo, and A. V. Babanin, 2012: The effect of wave-induced turbulence on the ocean mixed layer during tropical cyclones: Field observations on the Australian North-West Shelf. *J. Geophys. Res.*, **117**, C00J24, doi:10.1029/2011JC007780.
- Van Roekel, L. P., B. Fox-Kemper, P. P. Sullivan, P. E. Hamlington, and S. R. Haney, 2012: The form and orientation of Langmuir cells for misaligned winds and waves. *J. Geophys. Res.*, **117**, C05001, doi:10.1029/2011JC007516.
- Wallace, D. W. R., and C. D. Wirick, 1992: Large air–sea gas fluxes associated with breaking waves. *Nature*, **356**, 694–696, doi:10.1038/356694a0.
- Walsh, E. J., D. W. Hancock, D. E. Hines, R. N. Swift, and J. F. Scott, 1985: Directional wave spectra measured with the surface contour radar. *J. Phys. Oceanogr.*, **15**, 566–592, doi:10.1175/1520-0485(1985)015<0566:DWSMWT>2.0.CO;2.
- Webb, A., and B. Fox-Kemper, 2011: Wave spectral moments and Stokes drift estimation. *Ocean Modell.*, **40**, 273–288, doi:10.1016/j.ocemod.2011.08.007.
- Young, I. R., 2003: A review of the sea state generated by hurricanes. *Mar. Struct.*, **16**, 201–218, doi:10.1016/S0951-8339(02)00054-0.
- , 2006: Directional spectra of hurricane wind waves. *J. Geophys. Res.*, **111**, C08020, doi:10.1029/2006JC003540.